Waveform Inversion with a Data Driven Estimate of the Internal Wave*

Liliana Borcea[†], Josselin Garnier[‡], Alexander V. Mamonov[§], and Jörn Zimmerling[¶]

Abstract. We study an inverse problem for the wave equation, concerned with estimating the wave speed from data gathered by an array of sources and receivers that emit probing signals and measure the resulting waves. The typical approach to solving this problem is a nonlinear least squares minimization of the data misfit, over a search space. There are two main impediments to this approach, which manifest as multiple local minima of the objective function: The nonlinearity of the mapping from the wave speed to the data, which accounts for multiple scattering effects, and poor knowledge of the kinematics (smooth part of the wave speed), which causes cycle skipping. We show that the nonlinearity can be mitigated using a data driven estimate of the wave field at points inside the medium, also known as the "internal wave field." This leads to improved performance of the inversion for a reasonable initial guess of the kinematics.

Key words. inverse wave scattering, data driven, reduced order modeling, Lippmann–Schwinger integral equation, internal wave

MSC codes. 35L05, 65K10, 45Q05

DOI. 10.1137/22M1517342

1. Introduction. Inverse wave scattering is concerned with inferring properties of an inaccessible medium using remote sensors that emit probing signals and measure the generated
waves. It is an important technology in nondestructive evaluation of materials, exploration
geophysics, medical imaging with ultrasound, underwater sonar, radar imaging, etc. We consider scalar (sound) waves in a medium with constant mass density, so the unknown is the
wave speed c(x). The data are gathered by an array of m co-located sources and receivers.
The sources probe the medium sequentially with a signal, and the receivers record the generated wave. These recordings are organized in the time t dependent $m \times m$ array response
matrix $\mathcal{M}(t)$, the data for estimating c(x).

Received by the editors August 22, 2022; accepted for publication (in revised form) November 4, 2022; published electronically February 7, 2023.

https://doi.org/10.1137/22M1517342

Funding: This material is based upon work supported by the Air Force Office of Scientific Research under award number FA9550-22-1-0077 to Borcea and Garnier, the U.S. Office of Naval Research under award number N00014-21-1- 2370 to Borcea and Mamonov and the National Science Foundation under Grant No. DMS-2110265 to Zimmerling.

[†]Department of Mathematics, University of Michigan, Ann Arbor, MI 48109 USA (borcea@umich.edu).

[‡]CMAP, CNRS, Ecole Polytechnique, Institut Polytechnique de Paris, 91128 Palaiseau Cedex, France (josselin.garnier@polytechnique.edu).

[§] Department of Mathematics, University of Houston, 3551 Cullen Boulevard Houston, TX 77204-3008 USA (mamonov@math.uh.edu).

Uppsala Universitet, Department of Information Technology, Division of Scientific Computing, 75105 Uppsala, Sweden (jorn.zimmerling@it.uu.se).

There is extensive literature on qualitative methods for inverse wave scattering, also known as imaging methods, that seek to estimate the support of the rough part of the wave speed, called the reflectivity, which causes wave back-scattering. The smooth part of c(x), which determines the kinematics of the wave propagation, is assumed known in imaging and, with few exceptions, it is taken as constant. The most popular imaging methods, like reverse time migration [3, 28] and the related filtered back-projection [14, 13], are based on the single scattering (Born) approximation, which linearizes the forward mapping from the reflectivity to the array response matrix. Approaches like the factorization method [23] and the linear sampling method [12], which use the nonlinear forward mapping, are developed mostly for time-harmonic waves and work best for large arrays that almost surround the imaging region.

The literature on quantitative estimation of both the smooth and the rough part of c(x), called "waveform inversion" in this paper, consists of mainly two approaches: (1) PDE driven nonlinear least squares minimization of the data misfit, known as full waveform inversion (FWI) [31] in the seismology literature, and (2) iterative methods that alternate between imaging the reflectivity and adjusting the kinematics [29, 28]. Both approaches suffer from the nonlinearity of the forward mapping $c(x) \mapsto \mathcal{M}(t)$, which accounts for multiple scattering effects. The mitigation of such effects remains an active topic of research [32, 30]. Poor knowledge of the kinematics is also problematic, because travel time errors that exceed half the period of the probing signal cause the "cycle skipping" phenomenon [31]. The mitigation of cycle skipping is of great interest in exploration geophysics. The growing literature on the topic consists of methods that use lower frequency and wide-azimuth data, if available [10, 26], as well as travel time tomography to improve the guess kinematics [25]. Alternative approaches are to measure the data misfit using the optimal transport metric [33] or to add systematically degrees of freedom in the optimization [21]. A very different inversion method has emerged recently in [9], where cycle skipping is mitigated using a data driven reduced order model (ROM) of the wave operator.

In this paper we also use tools from data driven reduced order modeling to mitigate multiple scattering effects in waveform inversion. The main idea is that the forward mapping, given by the Lippmann–Schwinger integral equation for the scattered field, can be linearized approximately with a data driven estimate of the internal wave. The accuracy of this estimate relies on having a reasonable guess of the kinematics, and it can be improved iteratively during the inversion.

Our data driven approximation of the internal wave is rooted in the construction of the ROM for the wave propagator operator, developed in [15, 16, 7]. This operator controls the evolution of the wave field at discrete and equidistant time instants, and its ROM analogue is a matrix with special algebraic structure, which can be computed from the array response matrix. The propagator ROM has been used for imaging in [16] and for the linearization of the mapping from the wave impedance to the array response matrix, in a medium with known kinematics, in [5, 6]. Data driven approximations of the internal wave in the spectral (Laplace) domain have been introduced recently for estimating the scattering potential in diffusive equations [4, 17]. Time domain approximations of the internal wave, of the kind used in this paper, have also been used for imaging in the time domain in [8]. In this paper we extend the ideas developed in these works to waveform inversion. We formulate and motivate a novel inversion algorithm and assess its performance with numerical simulations.

The paper is organized as follows: We begin in section 2 with the formulation of the problem, the data model, and the integral equation that defines the forward mapping. The nonlinearity in this equation is due to the internal wave, which we estimate in section 3. The inversion algorithm is given in section 4, and the results of the numerical simulations are in section 5. We end with a summary in section 6.

- **2. Formulation of the problem.** Here we formulate mathematically the waveform inversion problem. We give first, in section 2.1, the model of the array response matrix $\mathcal{M}(t)$. Then, we explain in section 2.2 that if the medium near the sensors is known, which is typical in most applications, $\mathcal{M}(t)$ can be mapped to a new "data matrix" $\mathbf{D}(t)$. This mapping can be computed and there is no loss of information when working with $\mathbf{D}(t)$. The advantage is that we can get from $\mathbf{D}(t)$ an estimate of the internal wave, as explained in section 3. This is used for linearizing approximately the forward mapping $c(\mathbf{x}) \mapsto \mathbf{D}(t)$ defined in section 2.3.
- **2.1.** Mathematical model of the array response matrix. Suppose that the sources and receivers are point-like, at locations x_s , for s = 1, ..., m, and the probing signal is f(t), with support in the interval $(-t_f, t_f)$. The wave field generated by the sth excitation is denoted by $p^{(s)}(t, x)$. It is the solution of the wave equation

(2.1)
$$\left[\partial_t^2 - c^2(\boldsymbol{x})\Delta\right] p^{(s)}(t,\boldsymbol{x}) = f(t)\delta_{\boldsymbol{x}_s}(\boldsymbol{x}), \quad t \in \mathbb{R}, \ \boldsymbol{x} \in \Omega,$$

with quiescent initial condition

(2.2)
$$p^{(s)}(t, \boldsymbol{x}) \equiv 0, \quad t < -t_f, \ \boldsymbol{x} \in \Omega.$$

Here $\delta_{\boldsymbol{x}_s}(\boldsymbol{x})$ denotes the Dirac delta at \boldsymbol{x}_s , and Ω is a bounded, simply connected domain in \mathbb{R}^d , for $d \in \{2,3\}$. The methodology works the same for any homogeneous boundary conditions at $\partial\Omega$. We assume henceforth that $\partial\Omega$ is the union of a sound soft boundary $\partial\Omega_D$ and a sound hard boundary $\partial\Omega_N$, i.e., for all $t \in \mathbb{R}$ we have

(2.3)
$$[1_{\partial\Omega_D}(\boldsymbol{x}) + 1_{\partial\Omega_N}(\boldsymbol{x})\partial_n] p^{(s)}(t,\boldsymbol{x}) = 0, \quad \boldsymbol{x} \in \partial\Omega = \partial\Omega_D \cup \partial\Omega_N.$$

Here ∂_n denotes the normal derivative and $1_{\Gamma}(x)$ is the indicator function of a set $\Gamma \subset \mathbb{R}^d$, equal to 1 when $x \in \Gamma$ and zero otherwise.

Remark 2.1. The boundary $\partial\Omega$ may be physical or it can be introduced mathematically using the hyperbolicity of the problem, the finite wave speed, and the finite duration T of the measurements. That is to say, if the distance between $\partial\Omega$ and the set $\{x_s, s=1,\ldots,m\}$ is larger than $\max_{x\in\Omega} c(x)T$, then the recorded waves will not feel the boundary, and we can model it with whatever boundary conditions are most convenient for the computations. In our numerical simulations we use a physical sound hard boundary near the array, but the methodology extends verbatim to other setups.

The measurements are organized in the $m \times m$ time dependent array response matrix $\mathcal{M}(t)$, with entries defined by

(2.4)
$$\mathcal{M}^{(r,s)}(t) = -f'(-t) \star_t p^{(s)}(t, \mathbf{x}_r), \quad s, r = 1, \dots, m, \ t \in (0, T),$$

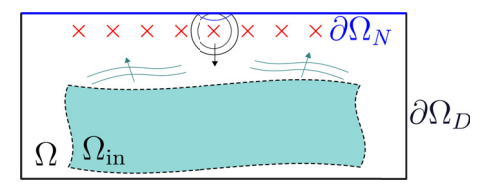


Figure 2.1. Illustration of the setup: An array of co-located sources and receivers (indicated with red crosses) probes a medium with incident waves and measures the backscattered waves. The unknown medium is in the remote, inaccessible subdomain Ω_{in} shown in blue.

where -f'(-t) is the derivative of the time reversed emitted signal and \star_t denotes convolution in time. Note that convolving the recorded wave signal with f(-t) is common in radar, sonar, and echography. In particular, in radar, the balance between the limited power of transmitters and the need for high signal to noise ratios requires using long probing signals f(t), like linear frequency modulated chirps, instead of short pulses. To improve the resolution of imaging, the generated waves $p^{(s)}(t, \mathbf{x}_r)$ are compressed in time by the "pulse compression" processing $f(-t)\star_t p^{(s)}(t,\boldsymbol{x}_r)$. Mathematically, this is equivalent to working with the wave generated by the source signal

$$(2.5) F(t) = f(-t) \star_t f(t),$$

which is of short duration. In (2.4) we convolve the wave with -f'(-t) instead of f(-t), so the resulting wave corresponds to the source signal F'(t). This is to facilitate a Duhamel principle type transformation of the inhomogeneous equation (2.1) to a homogeneous one, where the forcing is mapped to the initial state of the wave.

Let henceforth supp $(F) \subset (-t_F, t_F)$, and assume that the medium is known and homogeneous near the array, with constant wave speed \bar{c} . This assumption holds in most applications and by near we mean within a distance of order $\bar{c}t_F$ from the array. The unknown variations of $c(\mathbf{x})$ are supported in the inaccessible subdomain $\Omega_{\rm in} \subset \Omega$, as illustrated in Figure 2.1. We suppose that $\Omega_{\rm in}$ does not intersect $\partial \Omega_N$.

2.2. The new data matrix. From the mathematical point of view, it is convenient to work with a wave operator that is symmetric with respect to the $L^2(\Omega)$ inner product. Thus, we define the new wave field

(2.6)
$$P^{(s)}(t, \boldsymbol{x}) = -\frac{\bar{c}}{c(\boldsymbol{x})} f'(-t) \star_t p^{(s)}(t, \boldsymbol{x}),$$

which satisfies the initial boundary value problem

(2.7)
$$\left[\partial_t^2 + A(c)\right] P^{(s)}(t, \boldsymbol{x}) = F'(t)\delta_{\boldsymbol{x}_s}(\boldsymbol{x}), \qquad t \in \mathbb{R}, \ \boldsymbol{x} \in \Omega,$$

(2.7)
$$\left[\partial_t^2 + A(c) \right] P^{(s)}(t, \boldsymbol{x}) = F'(t) \delta_{\boldsymbol{x}_s}(\boldsymbol{x}), \qquad t \in \mathbb{R}, \ \boldsymbol{x} \in \Omega,$$
(2.8)
$$P^{(s)}(t, \boldsymbol{x}) \equiv 0, \qquad t < -t_F, \ \boldsymbol{x} \in \Omega,$$

(2.9)
$$[1_{\partial\Omega_D}(\boldsymbol{x}) + 1_{\partial\Omega_N}(\boldsymbol{x})\partial_n] P^{(s)}(t,\boldsymbol{x}) = 0, \qquad t \in \mathbb{R}, \ \boldsymbol{x} \in \partial\Omega,$$

with self-adjoint and positive definite operator A(c), acting on test functions $\Phi(x)$ as

(2.10)
$$A(c)\Phi(\mathbf{x}) = -c(\mathbf{x})\Delta[c(\mathbf{x})\Phi(\mathbf{x})].$$

For our purpose, it is useful to have a homogeneous wave equation, so we map the source term in (2.7) to an initial condition. We can think of this mapping as a Duhamel principle, although it is not in the usual form [22]. It amounts to working with the even in time wave field

(2.11)
$$W^{(s)}(t, \mathbf{x}) = P^{(s)}(t, \mathbf{x}) + P^{(s)}(-t, \mathbf{x}),$$

which, as shown in Appendix A, solves the initial boundary value problem

(2.12)
$$\left[\partial_t^2 + A(c)\right] W^{(s)}(t, \boldsymbol{x}) = 0, \qquad t > 0, \boldsymbol{x} \in \Omega,$$
(2.13)
$$W^{(s)}(0, \boldsymbol{x}) = \varphi^{(s)}(\boldsymbol{x}), \qquad \boldsymbol{x} \in \Omega.$$

$$(2.13) W(s)(0, \mathbf{x}) = \varphi(s)(\mathbf{x}), \mathbf{x} \in \Omega,$$

(2.14)
$$\partial_t W^{(s)}(0, \boldsymbol{x}) = 0, \qquad \boldsymbol{x} \in \Omega,$$

$$[1_{\partial\Omega_D}(\boldsymbol{x}) + 1_{\partial\Omega_N}(\boldsymbol{x})\partial_n]W^{(s)}(t,\boldsymbol{x}) = 0, \qquad t \ge 0, \ \boldsymbol{x} \in \partial\Omega.$$

The source term in (2.7) is mapped to the initial condition in (2.13), given by

(2.16)
$$\varphi^{(s)}(\boldsymbol{x}) = \widehat{F}[\sqrt{A(c)}]\delta_{\boldsymbol{x}_s}(\boldsymbol{x}),$$

where the hat denotes the Fourier transform and functions of the operator A(c) are defined using its spectral decomposition: If $\{\theta_j\}_{j\geq 1}$ are the eigenvalues of A(c) and $\{y_j(x)\}_{j\geq 1}$ are the eigenfunctions, which form an orthonormal basis of $L^2(\Omega)$ with the homogeneous boundary conditions, then a function ψ of A(c) is the operator with eigenvalues $\{\psi(\theta_i)\}_{i\geq 1}$ and eigenfunctions $\{y_j(\boldsymbol{x})\}_{j>1}$.

It is important to point out that there is no loss of information when working with $W^{(s)}(t, \boldsymbol{x})$. Indeed, due to the initial condition (2.8), we have

(2.17)
$$W^{(s)}(t, \mathbf{x}) = P^{(s)}(t, \mathbf{x}), \qquad t \ge t_F.$$

Moreover, by the hyperbolicity of the wave equation, the wave $W^{(s)}(t, \boldsymbol{x})$ is supported near the array at $|t| < t_F$, and it can be computed using the constant wave speed \bar{c} there. Thus, we can define the "data matrix" D(t), with entries

(2.18)
$$D^{(r,s)}(t) = W^{(s)}(t, \boldsymbol{x}_r) = \mathcal{M}^{(r,s)}(t) + \mathcal{M}^{(r,s)}(-t), \qquad t > 0, \ r, s = 1, \dots, m,$$

where the last term contributes only at $0 \le t < t_F$ and can be computed.

The advantage of working with the formulation (2.12)–(2.15) is that we can use operator calculus to write the solution as

$$(2.19) W(s)(t, \boldsymbol{x}) = \cos\left[t\sqrt{A(c)}\right]\varphi^{(s)}(\boldsymbol{x}).$$

Moreover, we can use the trigonometric identity

$$\cos[(t + \Delta t)\alpha] + \cos[(t - \Delta t)\alpha] = 2\cos(\Delta t\alpha)\cos(t\alpha) \quad \forall \alpha \in \mathbb{R}$$

and the definition of $\cos[t\sqrt{A(c)}]$ to obtain the exact time stepping relation

(2.20)
$$W^{(s)}(t + \Delta t, \mathbf{x}) = 2\cos\left[\Delta t \sqrt{A(c)}\right] W^{(s)}(t, \mathbf{x}) - W^{(s)}(t - \Delta t, \mathbf{x})$$

for any t and $\Delta t > 0$. This is an important tool for the ROM construction and the estimation of the internal wave in section 3.

2.3. The forward mapping. The next proposition defines the forward mapping $c(\boldsymbol{x}) \mapsto \boldsymbol{D}(t)$ using a Lippmann–Schwinger type integral equation for the scattered wave field. This field is given by the difference between the wave $W^{(s)}(t,\boldsymbol{x})$ in the unknown medium and the reference wave

(2.21)
$$W^{(s)}(t, \boldsymbol{x}; c_{\text{ref}}) = \cos\left[t\sqrt{A(c_{\text{ref}})}\right]\varphi^{(s)}(\boldsymbol{x}),$$

calculated with the wave speed $c_{ref}(\boldsymbol{x})$, our guess of $c(\boldsymbol{x})$.

Note that we use henceforth the following notation convention: To distinguish the fields calculated with an incorrect wave speed, like $c_{\text{ref}}(\boldsymbol{x})$, from the fields in the true medium, we introduce the extra argument c_{ref} . Thus, $W^{(s)}(t,\boldsymbol{x})$ and $\boldsymbol{D}(t)$ denote the wave and data in the true medium and $W^{(s)}(t,\boldsymbol{x};c_{\text{ref}})$ and $\boldsymbol{D}(t;c_{\text{ref}})$ are the analogues in the reference medium.

Proposition 2.2. Let $G(t, \mathbf{x}, \mathbf{x}'; c_{ref})$ denote the causal Green's function in the reference medium, the solution of the initial boundary value problem

$$\left[\partial_t^2 + A(c_{ref})\right] G(t, \boldsymbol{x}, \boldsymbol{x}'; c_{ref}) = \delta'(t) \delta_{\boldsymbol{x}'}(\boldsymbol{x}), \qquad t \in \mathbb{R}, \ \boldsymbol{x} \in \Omega,$$

(2.23)
$$G(t, \boldsymbol{x}, \boldsymbol{x}'; c_{ref}) \equiv 0, \qquad t < 0, \ \boldsymbol{x} \in \Omega,$$

$$[1_{\partial\Omega_{D}}(\boldsymbol{x}) + 1_{\partial\Omega_{N}}(\boldsymbol{x})\partial_{n}]G(t,\boldsymbol{x},\boldsymbol{x}';c_{ref}) = 0, \qquad t \in \mathbb{R}, \ \boldsymbol{x} \in \partial\Omega.$$

The mapping $c(\mathbf{x}) \mapsto \mathbf{D}(t)$ is defined componentwise by

(2.25)
$$D^{(r,s)}(t) = D^{(r,s)}(t; c_{\text{ref}}) + \int_{0}^{t} dt' \int_{\Omega} d\boldsymbol{x} \, \rho(\boldsymbol{x}) \partial_{t'} W^{(s)}(t', \boldsymbol{x}) G(t - t', \boldsymbol{x}, \boldsymbol{x}_{r}; c_{\text{ref}})$$

for r, s = 1, ..., m and t > 0, where $D^{(r,s)}(t; c_{ref}) = W^{(s)}(t, \boldsymbol{x}_r; c_{ref})$ and

(2.26)
$$\rho(\mathbf{x}) = \frac{c^2(\mathbf{x}) - c_{\text{ref}}^2(\mathbf{x})}{c(\mathbf{x})c_{\text{ref}}(\mathbf{x})}.$$

The proof of this proposition is in Appendix B. Note that the forward map is nonlinear, not only because of the definition of $\rho(\mathbf{x})$ in terms of $c(\mathbf{x})$, but also because the right hand side involves the internal wave $W^{(s)}(t,\mathbf{x})$. This depends on the unknown $c(\mathbf{x})$ in a complicated way, as seen from (2.19). Our goal is to obtain an estimate of this internal wave, called $\widetilde{W}^{(s)}(t,\mathbf{x};c_{\text{ref}})$, and use it to define the linear mapping $\rho(\mathbf{x}) \mapsto \mathbf{L}[\rho](t;c_{\text{ref}})$, defined componentwise by

(2.27)
$$L^{(r,s)}[\rho](t;c_{\text{ref}}) = \int_0^t dt' \int_{\Omega} d\boldsymbol{x} \, \rho(\boldsymbol{x}) \partial_{t'} \widetilde{W}^{(s)}(t',\boldsymbol{x};c_{\text{ref}}) G(t-t',\boldsymbol{x},\boldsymbol{x}_r;c_{\text{ref}}).$$

The inversion can then be carried out via the linear least squares minimization

(2.28)
$$\widetilde{\rho}(\boldsymbol{x}) = \underset{\rho_{\mathcal{R}}}{\operatorname{argmin}} \int_{0}^{T} dt \, \|\boldsymbol{D}(t) - \boldsymbol{D}(t; c_{\text{ref}}) - \boldsymbol{L}[\rho_{\mathcal{R}}](t; c_{\text{ref}})\|_{F}^{2} + \text{ regularization},$$

where $\rho_{\mathcal{R}}(\boldsymbol{x})$ lies in some search space \mathcal{R} and $\|\cdot\|_F$ denotes the Frobenius norm. The estimated wave speed is determined by the minimizer (2.28), according to (2.26), as follows:

(2.29)
$$\widetilde{c}(\boldsymbol{x}) = \frac{c_{\text{ref}}(\boldsymbol{x})}{2} \left[\widetilde{\rho}(\boldsymbol{x}) + \sqrt{4 + \widetilde{\rho}^2(\boldsymbol{x})} \right].$$

Remark 2.3. While the internal wave $W^{(s)}(t, \boldsymbol{x})$ depends on the true and unknown $c(\boldsymbol{x})$, its estimate $\widetilde{W}^{(s)}(t, \boldsymbol{x}; c_{\text{ref}})$ depends both on $c(\boldsymbol{x})$, because it is calculated from the $c(\boldsymbol{x})$ dependent data, and on $c_{\text{ref}}(\boldsymbol{x})$. According to our notation convention, we indicate the latter dependence by adding c_{ref} to its arguments. The dependence of $\widetilde{W}^{(s)}(t, \boldsymbol{x}; c_{\text{ref}})$ on c_{ref} is different than that of the wave $W^{(s)}(t, \boldsymbol{x}; c_{\text{ref}})$ in the reference medium, as we explain in the next section and illustrate later with numerical simulations. It is mostly the smooth part of c_{ref} that affects $\widetilde{W}^{(s)}(t, \boldsymbol{x}; c_{\text{ref}})$, whereas $W^{(s)}(t, \boldsymbol{x}; c_{\text{ref}})$ is sensitive to both the smooth and rough parts of c_{ref} .

3. Estimation of the internal wave. Before explaining how we compute $\widetilde{W}^{(s)}(t, \boldsymbol{x}; c_{\text{ref}})$ for a given $c_{\text{ref}}(\boldsymbol{x})$, let us write the internal wave as the time convolution (see Appendix C)

(3.1)
$$W^{(s)}(t, \boldsymbol{x}) = f(t) \star_t u^{(s)}(t, \boldsymbol{x})$$

of the even pulse

(3.2)
$$f(t) = \int_{-\infty}^{\infty} \frac{d\omega}{2\pi} \sqrt{\widehat{F}(\omega)} \cos(\omega t),$$

with Fourier transform $\widehat{\mathfrak{f}}(\omega) = \sqrt{\widehat{F}(\omega)}$, and the wave field

(3.3)
$$u^{(s)}(t, \mathbf{x}) = \cos\left[t\sqrt{A(c)}\right]u_0^{(s)}(\mathbf{x}),$$

that satisfies the same homogeneous wave equation as $W^{(s)}(t,x)$, but has the initial state

(3.4)
$$u^{(s)}(0, \mathbf{x}) = u_0^{(s)}(\mathbf{x}) = \widehat{\mathfrak{f}}[\sqrt{A(c)}]\delta_{\mathbf{x}_c}(\mathbf{x}).$$

The advantage of expression (3.1) is twofold: First, we have

(3.5)
$$\partial_t W^{(s)}(t, \boldsymbol{x}) = f'(t) \star_t u^{(s)}(t, \boldsymbol{x}),$$

where the time derivative is shifted to the known pulse f(t), i.e., we do not need to estimate the time derivative of the internal wave (3.3), just the wave itself. Second, from discrete, equidistant time samples of the data, at interval² τ ,

(3.6)
$$D_j = D(j\tau), \quad j = 0, \dots, 2(n-1),$$

and we can estimate $u^{(s)}(t, \mathbf{x})$ at time $t \in (0, T)$, with $T = (n - 1)\tau$.

¹Observe from (2.5) that the Fourier transform $\widehat{F}(\omega)$ of F(t) is nonnegative.

²The interval τ should be chosen close to the Nyquist sampling rate for the highest frequency in the essential support of $\widehat{F}(\omega)$, defined, for example, using a 6dB power drop from the peak value. This ensures a stable and more accurate estimation of the internal wave. A smaller τ requires regularization, as we explain later, and a larger τ gives a worse estimate of the wave.

Remark 3.1. To estimate the internal wave at $t \in (0,T)$, as needed in (2.28), we use measurements up to 2T. This is due to the back-scattering data acquisition setup: The waves make a round-trip from the sources in the array to points inside the medium, where they scatter, and then travel back to the array, where they are measured. Thus, data (3.6) carry information about the parts of the medium reached by the waves up to travel time T.

Our estimate of the internal wave is based on a ROM for the evolution equation satisfied by the snapshots

(3.7)
$$u_j(x) = (u^{(1)}(j\tau, x), \dots, u^{(m)}(j\tau, x)), \quad j \ge 0$$

These are m dimensional row vector fields with components given by the waves (3.3) evaluated at the instants $t = j\tau$ for all the sources in the array. They evolve from one instant to the next according to the time stepping scheme

(3.8)
$$u_{j+1}(x) = 2\mathcal{P}u_j(x) - u_{|j-1|}(x), \quad j \ge 0, \ x \in \Omega,$$

with initial condition

(3.9)
$$u_0(x) = \widehat{\mathfrak{f}}[\sqrt{A(c)}] (\delta_{x_1}(x), \dots, \delta_{x_m}(x)), \qquad x \in \Omega.$$

The evolution is driven by the propagator operator $\mathcal{P} = \cos[\tau \sqrt{A(c)}]$, and the time stepping scheme is exact, i.e., it does not stem from a finite difference approximation of ∂_t^2 . It is derived from (2.20) evaluated at $t = j\tau$ and $\Delta t = \tau$.

The ROM introduced and analyzed in [15, 5, 7] can be understood as the Galerkin projection of (3.8)–(3.9) on the space $\mathscr S$ spanned by the first n snapshots. We review it briefly in section 3.1, and then use it in section 3.2 to estimate the internal wave.

3.1. Data driven ROM. Let us assume that \mathscr{S} has dimension nm, which is typically the case if the step size τ is chosen properly. Otherwise, the construction below requires regularization (see section 4).

If we gather the first n snapshots (3.7) in the nm dimensional row vector field

(3.10)
$$U(x) = (u_0(x), \dots, u_{n-1}(x)),$$

we have, in linear algebra notation, $\mathscr{S} = \text{range}[\boldsymbol{U}(\boldsymbol{x})]$. To write the Galerkin projection of (3.8)–(3.9) we use an orthonormal basis of \mathscr{S} , stored in the nm dimensional row vector field $\boldsymbol{V}(\boldsymbol{x})$ and defined by the Gram–Schmidt orthogonalization procedure

(3.11)
$$V(x) = (\mathbf{v}_0(x), \dots, \mathbf{v}_{n-1}(x)) = U(x)R^{-1}.$$

This procedure is causal, meaning that

(3.12)
$$\mathbf{v}_{j}(\mathbf{x}) \in \text{span}\{\mathbf{u}_{0}(\mathbf{x}), \dots, \mathbf{u}_{j}(\mathbf{x})\}, \quad j = 0, \dots, n-1,$$

so the $nm \times nm$ matrix \mathbf{R}^{-1} , and therefore \mathbf{R} , are block upper triangular, with $m \times m$ blocks. The orthonormality of the basis means that

(3.13)
$$\int_{\Omega} d\boldsymbol{x} \, \boldsymbol{V}^{T}(\boldsymbol{x}) \boldsymbol{V}(\boldsymbol{x}) = \boldsymbol{I},$$

where I is the $nm \times nm$ identity matrix.

The projection of (3.8)–(3.9) gives the algebraic (ROM) time stepping scheme [15, 5, 7],

(3.14)
$$\boldsymbol{u}_{j+1}^{\text{ROM}} = 2\boldsymbol{\mathcal{P}}^{\text{ROM}} \boldsymbol{u}_{j}^{\text{ROM}} - \boldsymbol{u}_{|j-1|}^{\text{ROM}}, \qquad j \ge 0,$$

where \mathcal{P}^{ROM} is the $nm \times nm$ ROM propagator matrix, defined by

(3.15)
$$\mathcal{P}^{\text{ROM}} = \int_{\Omega} d\boldsymbol{x} \, \boldsymbol{V}^{T}(\boldsymbol{x}) \mathcal{P} \boldsymbol{V}(\boldsymbol{x}) = \boldsymbol{R}^{-1^{T}} \left[\int_{\Omega} d\boldsymbol{x} \, \boldsymbol{U}^{T}(\boldsymbol{x}) \mathcal{P} \boldsymbol{U}(\boldsymbol{x}) \right] \boldsymbol{R}^{-1},$$

and the ROM snapshots are $nm \times m$ matrices, given by

(3.16)
$$\mathbf{u}_{j}^{\text{ROM}} = \int_{\Omega} d\mathbf{x} \, \mathbf{V}^{T}(\mathbf{x}) \mathbf{u}_{j}^{\text{Gal}}(\mathbf{x}), \qquad j \geq 0.$$

Here $u_j^{\text{Gal}}(\boldsymbol{x})$ is the Galerkin approximation of the snapshots (3.7), defined in the standard way, as the linear combination of the components of $U(\boldsymbol{x})$, which span \mathscr{S} ,

(3.17)
$$\boldsymbol{u}_{j}^{\mathrm{Gal}}(\boldsymbol{x}) = \boldsymbol{U}(\boldsymbol{x})\boldsymbol{g}_{j},$$

with coefficient matrices $\boldsymbol{g}_{i} \in \mathbb{R}^{nm \times m}$ calculated so that the residual

(3.18)
$$u_{j+1}^{Gal}(x) + u_{j-1}^{Gal}(x) - 2\mathcal{P}u_{j}^{Gal}(x) = U(x)(g_{j+1} + g_{j-1}) - 2\mathcal{P}U(x)g_{j},$$

is orthogonal to \mathscr{S} . This gives

(3.19)
$$M(g_{j+1} + g_{j-1}) - 2Sg_j = 0, \quad j \ge 0,$$

where M and S are the Galerkin "mass" and "stiffness" matrices

(3.20)
$$M = \int_{\Omega} d\mathbf{x} U^{T}(\mathbf{x}) U(\mathbf{x}), \qquad S = \int_{\Omega} d\mathbf{x} U^{T}(\mathbf{x}) \mathcal{P} U(\mathbf{x}).$$

Substituting (3.17) in (3.16) and using that (3.11) is equivalent to

$$(3.21) U(x) = V(x)R,$$

we get that the ROM snapshots are

(3.22)
$$\mathbf{u}_{j}^{\text{ROM}} = \int_{\Omega} d\mathbf{x} \, \mathbf{V}^{T}(\mathbf{x}) \mathbf{V}(\mathbf{x}) \mathbf{R} \mathbf{g}_{j} = \mathbf{R} \mathbf{g}_{j}, \qquad j \geq 0.$$

What we have described so far follows the standard procedure for computing model driven Galerkin projection ROMs [2, 11, 20]. However, there are two essential points to make:

- 1. The snapshots stored in U(x) are unknown in inverse scattering, so the ROM cannot be computed as above. In fact, as explained below, our ROM is data driven, i.e., it can be computed from the data matrices $\{D_j\}_{j=0}^{2n-1}$.
- 2. Because the time stepping scheme (3.8) is exact, our ROM has better approximation properties than the usual ROMs for the wave equation [19, 24, 20], which use either the derivative ∂_t^2 or a finite difference approximation of it. This is important for the estimation of the internal wave.

We begin the explanation of these two points with the following observation: The definition of the approximation space \mathscr{S} and (3.8)–(3.9) imply that the residual (3.18) vanishes for the first n time instants. Consequently, the Galerkin approximation at these instants is exact,

(3.23)
$$u_j^{\text{Gal}}(x) = U(x)g_j = u_j(x), \quad j = 0, ..., n-1,$$

or, equivalently, the first n Galerkin coefficient matrices are trivial,

(3.24)
$$\mathbf{g}_{j} = \mathbf{e}_{j}, \quad j = 0, \dots, n-1.$$

Here e_i are the $nm \times m$ block columns of the $nm \times nm$ identity matrix I, i.e.,

$$I = (e_0, \ldots, e_{n-1}).$$

Next, we note that the Galerkin mass matrix defined in (3.20) can be computed as follows: Let M be organized in $m \times m$ blocks $M_{i,j}$, indexed by the pair (i,j), with $i,j=0,\ldots,n-1$. The entries in the (i,j)th block are denoted by $M_{i,j}^{(r,s)}$, with $r,s=1,\ldots,m$, and are determined by the data matrices (3.6) as follows:

$$M_{i,j}^{(r,s)} = \int_{\Omega} d\boldsymbol{x} \, u^{(r)}(i\tau, \boldsymbol{x}) u^{(s)}(j\tau, \boldsymbol{x})$$

$$= \int_{\Omega} d\boldsymbol{x} \, \cos\left[i\tau\sqrt{A(c)}\right] \widehat{\mathfrak{f}}\left[\sqrt{A(c)}\right] \delta_{\boldsymbol{x}_{r}}(\boldsymbol{x}) \cos\left[j\tau\sqrt{A(c)}\right] \widehat{\mathfrak{f}}\left[\sqrt{A(c)}\right] \delta_{\boldsymbol{x}_{s}}(\boldsymbol{x})$$

$$= \int_{\Omega} d\boldsymbol{x} \, \delta_{\boldsymbol{x}_{r}}(\boldsymbol{x}) \cos\left[i\tau\sqrt{A(c)}\right] \cos\left[j\tau\sqrt{A(c)}\right] \left(\widehat{\mathfrak{f}}\left[\sqrt{A(c)}\right]\right)^{2} \delta_{\boldsymbol{x}_{s}}(\boldsymbol{x})$$

$$= \frac{1}{2} \int_{\Omega} d\boldsymbol{x} \, \delta_{\boldsymbol{x}_{r}}(\boldsymbol{x}) \left\{\cos\left[(i+j)\tau\sqrt{A(c)}\right] + \cos\left[(i-j)\tau\sqrt{A(c)}\right]\right\} \varphi^{(s)}(\boldsymbol{x})$$

$$= \frac{1}{2} \left[W^{(s)}((i+j)\tau, \boldsymbol{x}_{r}) + W^{(s)}(|i-j|\tau, \boldsymbol{x}_{r})\right]$$

$$= \frac{1}{2} \left[D_{i+j}^{(r,s)} + D_{|i-j|}^{(r,s)}\right].$$
(3.25)

The first equality in this equation is by definition (3.20), the second equality is by definitions (3.3)–(3.4), the third equality is because A(c) is self-adjoint and functions of A(c) commute, the fourth equality uses definitions (2.16) and (3.2) as well as (2.20) evaluated at $t = i\tau$ and $\Delta t = j\tau$, the fifth equality uses definition (2.19), and the last equality is by definition (2.18).

Similarly, the entries of the stiffness matrix are, for block indexes i, j = 0, ..., n-1 and for entry indexes r, s = 1, ..., m in the blocks,

$$S_{i,j}^{(r,s)} = \int_{\Omega} d\boldsymbol{x} \, u^{(r)}(i\tau, \boldsymbol{x}) \boldsymbol{\mathcal{P}} u^{(s)}(j\tau, \boldsymbol{x})$$

$$= \frac{1}{2} \int_{\Omega} d\boldsymbol{x} \, u^{(r)}(i\tau, \boldsymbol{x}) \left\{ u^{(r)}[(j+1)\tau, \boldsymbol{x}] + u^{(r)}[|j-1|\tau, \boldsymbol{x}] \right\}$$

$$= \frac{1}{4} \left[D_{i+j+1}^{(r,s)} + D_{|i-j-1|}^{(r,s)} + D_{|i-j+1|}^{(r,s)} + D_{|i-j+1|}^{(r,s)} \right],$$
(3.26)

where the first equality is by definition (3.20), the second equality uses (3.8), and the last equality follows as in (3.25).

Note that the calculation of the mass matrix uses the data matrices $\{D_j\}_{j=0}^{2n-2}$, while the calculation of the stiffness matrix requires the extra matrix D_{2n-1} . Once we compute M and S, we can obtain from (3.19) all the Galerkin coefficient matrices g_j , for $j \geq n$, starting with the trivial ones given in (3.24). Next, substituting the Gram-Schmidt orthogonalization equation (3.21) in the definition (3.20) of the mass matrix, and recalling the orthonormality equation (3.13), we get

(3.27)
$$M = \mathbf{R}^T \int_{\Omega} d\mathbf{x} \, \mathbf{V}^T(\mathbf{x}) \mathbf{V}(\mathbf{x}) \, \mathbf{R} = \mathbf{R}^T \mathbf{R}.$$

Thus, \mathbf{R} can be computed from the data as the block Cholesky square root of \mathbf{M} . This gives the ROM snapshots (3.22). The ROM propagator is also data driven, by definitions (3.15) and (3.20),

$$\boldsymbol{\mathcal{P}}^{\text{ROM}} = \boldsymbol{R}^{-1^T} \boldsymbol{S} \boldsymbol{R}^{-1}.$$

Remark 3.2. There are various ways to compute the block Cholesky factorization (3.27). They differ in the computation of the diagonal blocks of \mathbf{R} , which involves taking the square root of an $m \times m$ symmetric and positive definite matrix. Any factorization should work, as long as it is used consistently throughout the inversion. We use [16, Algorithm 5.2], which takes the square root using the spectral decomposition of the matrix.

3.2. Data driven estimate of the internal wave. Ideally, the internal wave $u^{(s)}(t, \boldsymbol{x})$ would be given by the interpolation in t of the snapshots

(3.29)
$$u^{(s)}(j\tau, \boldsymbol{x}) = [\boldsymbol{V}(\boldsymbol{x})\boldsymbol{R}\boldsymbol{e}_j]_s = \sum_{q=0}^{j} [\mathbf{v}_q(\boldsymbol{x})\boldsymbol{R}_{q,j}]_s,$$

at indexes j and j+1 corresponding to the ends of the interval $[j\tau, (j+1)\tau]$ that contains t. Here $[\cdot]_s$ denotes the sth component and the right hand side is due to the Gram–Schmidt orthogonalization equations (3.11), (3.21) and the block upper triangular structure of \mathbf{R} , with nonzero $m \times m$ blocks denoted by $\mathbf{R}_{q,j}$ for indexes $0 \le q \le j \le n-1$.

Unfortunately, we only know the matrix \mathbf{R} in (3.29), the square root of the mass matrix \mathbf{M} computed from $\{\mathbf{D}_j\}_{j=0}^{2n-2}$ as in (3.25). We do not know $\mathbf{V}(\mathbf{x})$, whose orthonormal components span the unknown space \mathscr{S} . To estimate the internal wave, we replace $\mathbf{V}(\mathbf{x})$ by $\mathbf{V}(\mathbf{x}; c_{\text{ref}})$, the row vector field that stores the orthonormal basis of the space $\mathscr{S}(c_{\text{ref}})$, spanned by the snapshots in the reference medium with known wave speed $c_{\text{ref}}(\mathbf{x})$. This basis can be computed by solving the wave equation to get the nm dimensional row vector $\mathbf{U}(\mathbf{x}; c_{\text{ref}})$, the reference mass matrix $\mathbf{M}(c_{\text{ref}})$, and its block Cholesky square root $\mathbf{R}(c_{\text{ref}})$. Then, we have

(3.30)
$$V(x; c_{\text{ref}}) = U(x; c_{\text{ref}})R(c_{\text{ref}})^{-1},$$

and we estimate (3.29) by

$$(3.31) \qquad \widetilde{u}^{(s)}(j\tau, \boldsymbol{x}; c_{\text{ref}}) = \left[\boldsymbol{V}(\boldsymbol{x}; c_{\text{ref}}) \boldsymbol{R} \boldsymbol{e}_{j}\right]_{s} = \sum_{q=0}^{j} \left[\mathbf{v}_{q}(\boldsymbol{x}; c_{\text{ref}}) \boldsymbol{R}_{q, j}\right]_{s}$$

for j = 0, ..., n - 1 and s = 1, ..., m.

Why is this estimate of the internal wave a good choice? The next proposition states that it fits the data $\{D_j\}_{j=0}^{2n-2}$. Thus, it must be a better approximation of the internal wave than the reference wave used by the standard iterative algorithms, which does not fit the data. In our context, this reference wave is given by

(3.32)
$$u^{(s)}(j\tau, \mathbf{x}; c_{\text{ref}}) = [\mathbf{V}(\mathbf{x}; c_{\text{ref}})\mathbf{R}(c_{\text{ref}})\mathbf{e}_j]_s, \quad j = 0, \dots, n-1, \ s = 1, \dots, m.$$

Proposition 3.3. 1. The internal wave evaluated at $t = j\tau$, i.e., the snapshot (3.29), satisfies the data fit relations

(3.33)
$$D_j = \int_{\Omega} d\mathbf{x} \, \mathbf{u}_0^T(\mathbf{x}) \mathbf{u}_j(\mathbf{x}), \qquad j \ge 0.$$

We also have

(3.34)
$$D_{j+n-1} + D_{n-1-j} = 2 \int_{\Omega} dx \, u_{n-1}^{T}(x) u_{j}(x), \quad j = 0, \dots, n-1.$$

2. The estimate (3.31) of the internal wave also satisfies the data fit relations

(3.35)
$$\mathbf{D}_{j} = \int_{\Omega} d\mathbf{x} \, \widetilde{\mathbf{u}}_{0}^{T}(\mathbf{x}; c_{\text{ref}}) \widetilde{\mathbf{u}}_{j}(\mathbf{x}; c_{\text{ref}}),$$

(3.36)
$$\boldsymbol{D}_{j+n-1} + \boldsymbol{D}_{n-1-j} = 2 \int_{\Omega} d\boldsymbol{x} \, \widetilde{\boldsymbol{u}}_{n-1}^{T}(\boldsymbol{x}; c_{\text{ref}}) \widetilde{\boldsymbol{u}}_{j}(\boldsymbol{x}; c_{\text{ref}}), \qquad j = 0, \dots, n-1.$$

Here we denote, similar to the row vector field notation in (3.7),

$$\widetilde{\boldsymbol{u}}_{j}(\boldsymbol{x}; c_{\mathrm{ref}}) = (\widetilde{\boldsymbol{u}}^{(1)}(j\tau, \boldsymbol{x}; c_{\mathrm{ref}}), \dots, \widetilde{\boldsymbol{u}}^{(m)}(j\tau, \boldsymbol{x}; c_{\mathrm{ref}})), \qquad j = 0, \dots, n-1.$$

Before we give the proof, let us describe in more detail what the proposition says. Recall from (2.18), (3.1), and (3.6) that the entries of the $m \times m$ data matrices \mathbf{D}_i are

(3.37)
$$D_j^{(r,s)} = W^{(s)}(j\tau, \mathbf{x}_r) = \mathfrak{f}(t) \star_t u^{(s)}(t, \mathbf{x}_r)|_{t=j\tau}, \qquad r, s = 1, \dots, m.$$

The first point of the proposition is that these entries can be written as inner products of the components of the snapshots $u_j(x)$, for $j \ge 0$. This can be seen from the calculation of the mass and stiffness matrices in (3.25)–(3.26). We can also deduce directly from (2.16), (2.19), (3.3)–(3.4) and the definition of \hat{f} as the square root of \hat{F} that

$$D_{j}^{(r,s)} = W^{(s)}(j\tau, \boldsymbol{x}_{r}) = \int_{\Omega} d\boldsymbol{x} \, \delta_{\boldsymbol{x}_{r}}(\boldsymbol{x}) \cos\left[j\tau\sqrt{A(c)}\right] \widehat{F}[\sqrt{A(c)}] \delta_{\boldsymbol{x}_{s}}(\boldsymbol{x})$$

$$= \int_{\Omega} d\boldsymbol{x} \, \widehat{\mathfrak{f}}[\sqrt{A(c)}] \delta_{\boldsymbol{x}_{r}}(\boldsymbol{x}) \cos\left[j\tau\sqrt{A(c)}\right] \widehat{\mathfrak{f}}[\sqrt{A(c)}] \delta_{\boldsymbol{x}_{s}}(\boldsymbol{x})$$

$$= \int_{\Omega} d\boldsymbol{x} \, u_{0}^{(r)}(\boldsymbol{x}) u_{j}^{(s)}(\boldsymbol{x}), \qquad j \geq 0.$$

$$(3.38)$$

The third equality in this equation is because A(c) is self-adjoint and functions of A(c) commute.

The second point of the proposition is that when replacing $u_0^{(r)}(\boldsymbol{x})$ and $u_j^{(s)}(\boldsymbol{x})$ by $\widetilde{u}_0^{(r)}(\boldsymbol{x}; c_{\text{ref}})$ and $\widetilde{u}_j^{(s)}(\boldsymbol{x}; c_{\text{ref}})$ in (3.38), we match the data for $j = 0, \ldots, n-1$. Note that thanks to the causal definition of the orthonormal bases in $\boldsymbol{V}(\boldsymbol{x})$ and $\boldsymbol{V}(\boldsymbol{x}; c_{\text{ref}})$ and the assumption that $c(\boldsymbol{x}) = c_{\text{ref}}(\boldsymbol{x}) = \bar{c}$ within a distance of order $\bar{c}t_F$ from the array, we have

$$\widetilde{\mathbf{v}}_0(\boldsymbol{x}; c_{\text{ref}}) = \mathbf{v}_0(\boldsymbol{x}),$$

and therefore

$$\widetilde{\boldsymbol{u}}_0(\boldsymbol{x}; c_{\text{ref}}) = \boldsymbol{u}_0(\boldsymbol{x}) = \mathbf{v}_0(\boldsymbol{x}) \boldsymbol{R}_{0.0}.$$

At time instants $j\tau \gg t_F$ the estimated internal wave is different from the true one

(3.41)
$$\widetilde{u}_{j}^{(s)}(\boldsymbol{x}; c_{\text{ref}}) \neq u_{j}^{(s)}(\boldsymbol{x}) = \cos \left[j\tau \sqrt{A(c)} \right] u_{0}^{(s)}(\boldsymbol{x}),$$

and yet, when using it in (3.38), we get an exact data match for $j \le n-1$.

The proposition also shows that the data matrices D_n, \ldots, D_{2n-2} can be written as the difference of two terms: The first is an inner product of the components of $u_j(x)$, for $j = 0, \ldots, n-1$, and the second is given by the data matrices at the first n time instants. Both these terms are matched by the estimated internal wave. Therefore, we have an exact data match at instants $j\tau$, for $j = 0, \ldots, 2n-2$.

Proof of Proposition 3.3. Equation (3.33) is just (3.38) written in block form. If we restrict it to j = 0, ..., n-1, we also get it from (3.25) evaluated at i = 0 and j = 0, ..., n-1. In order to prove (3.34) we take i = n-1 and j = 0, ..., n-1 in (3.25) and get, in block form,

$$m{D}_{j+n-1} + m{D}_{n-1-j} = 2m{M}_{n-1,j} = 2\int_{\Omega} dm{x} \, m{u}_{n-1}^T(m{x}) m{u}_j(m{x}).$$

To complete the proof of the proposition we note that the estimate (3.31) satisfies

$$\begin{split} \int_{\Omega} d\boldsymbol{x} \, \widetilde{\boldsymbol{u}}_{q}^{T}(\boldsymbol{x}; c_{\text{ref}}) \widetilde{\boldsymbol{u}}_{j}(\boldsymbol{x}; c_{\text{ref}}) &= \boldsymbol{e}_{q}^{T} \boldsymbol{R}^{T} \int_{\Omega} d\boldsymbol{x} \, \boldsymbol{V}^{T}(\boldsymbol{x}; c_{\text{ref}}) \boldsymbol{V}(\boldsymbol{x}; c_{\text{ref}}) \, \boldsymbol{R} \boldsymbol{e}_{j} \\ &= \boldsymbol{e}_{q}^{T} \boldsymbol{R}^{T} \boldsymbol{R} \boldsymbol{e}_{j} = \boldsymbol{e}_{q} \boldsymbol{M} \boldsymbol{e}_{j} \\ &= \boldsymbol{e}_{q} \int_{\Omega} d\boldsymbol{x} \, \boldsymbol{U}^{T}(\boldsymbol{x}) \boldsymbol{U}(\boldsymbol{x}) \, \boldsymbol{e}_{j} \\ &= \int_{\Omega} d\boldsymbol{x} \, \boldsymbol{u}_{q}^{T}(\boldsymbol{x}) \boldsymbol{u}_{j}(\boldsymbol{x}) \end{split}$$

for $j, q = 0, \dots, n-1$. The statement of the proposition follows.

The calculation above shows that it is the factor \mathbf{R} in the estimate (3.31) that ensures the data fit. By equations (3.22) and (3.24), \mathbf{R} stores the first n ROM snapshots. The vector field $\mathbf{V}(\mathbf{x}; c_{\text{ref}})$ is used to map these snapshots from the algebraic ROM space to the physical space. As long as there is a difference between the data $\{\mathbf{D}_j\}_{j=0}^{2n-2}$ and the computed one in

the reference medium $\{D_j(c_{\text{ref}})\}_{j=0}^{2n-2}$, this is reflected in R and its reference analogue $R(c_{\text{ref}})$, so

$$\widetilde{u}^{(s)}(j\tau, \boldsymbol{x}; c_{\text{ref}}) = \left[\boldsymbol{V}(\boldsymbol{x}; c_{\text{ref}})\boldsymbol{R}\boldsymbol{e}_{j}\right]_{s} \neq u^{(s)}(j\tau, \boldsymbol{x}; c_{\text{ref}}) = \left[\boldsymbol{V}(\boldsymbol{x}; c_{\text{ref}})\boldsymbol{R}(c_{\text{ref}})\boldsymbol{e}_{j}\right]_{s}.$$

Numerical evidence and explicit analysis carried out in layered media and also in waveguides [8, Appendix A] show that $V(x; c_{ref})$ is largely insensitive to the rough part of $c_{ref}(x)$, i.e., the reflectivity, but it does depend on the smooth part of $c_{ref}(x)$, i.e., the kinematics. The implication is that the estimate (3.31) may display the correct scattering events, but these can be misplaced in Ω due to the travel times given by the incorrect kinematics.

Our inversion algorithm (see next section) recalculates $V(x; c_{\text{ref}})$ as we update the guess wave speed $c_{\text{ref}}(x)$. As long as the initial guess of the kinematics is not too far from the truth, it succeeds in giving a better estimate of c(x) than the traditional iterative algorithms that estimate the internal wave by $u^{(s)}(j\tau, x; c_{\text{ref}})$.

4. The inversion. Let us begin with a reformulation of Proposition 2.2 that is better suited for computations.

Proposition 4.1. The forward map $c(\mathbf{x}) \mapsto \rho(\mathbf{x}) \mapsto \mathbf{D}(t)$ defined in Proposition 2.2 for a given $c_{\text{ref}}(\mathbf{x})$ can be rewritten as

(4.1)
$$D^{(r,s)}(t) - D^{(r,s)}(t; c_{\text{ref}}) = \int_0^t dt' \int_{\Omega_{\text{in}}} d\boldsymbol{x} \, \rho(\boldsymbol{x}) u^{(s)}(t', \boldsymbol{x}) \partial_{t'} u^{(r)}(t', \boldsymbol{x}; c_{\text{ref}})$$

for r, s = 1, ..., m and t > 0.

The proof is in Appendix D and the main advantage of (4.1) over (2.25) is that we do not have to deal with the Green's function $G(t, \boldsymbol{x}, \boldsymbol{x}_r; c_{\text{ref}})$, which is difficult to compute. The convolution term f'(t) that appears in the expression (3.5) is now included in the factor $\partial_t u^{(r)}(t, \boldsymbol{x}; c_{\text{ref}})$, which can be easily computed.

We estimate first the function $\rho(\mathbf{x})$ by the minimizer of (2.28), and then the wave speed $c(\mathbf{x})$, using (2.29). The search space is

(4.2)
$$\mathcal{R} = \operatorname{span}\{\beta_j(\boldsymbol{x}), j = 1, \dots, N_\rho\},\$$

where $\{\beta_j(\boldsymbol{x})\}_{j=1}^{N_\rho}$ are user defined basis functions, so the search field is

(4.3)
$$\rho_{\mathcal{R}}(\boldsymbol{x}) = \sum_{j=1}^{N_{\rho}} \eta_{j} \beta_{j}(\boldsymbol{x})$$

with the unknown coefficients gathered in the column vector $\boldsymbol{\eta} = (\eta_1, \dots, \eta_{N_\rho})^T$. The linear map $\boldsymbol{\eta} \mapsto \rho_{\mathcal{R}} \mapsto \boldsymbol{L}[\rho_{\mathcal{R}}](t; c_{\text{ref}})$ that enters the expression of the objective function (2.28) is computed as

(4.4)
$$\mathbf{L}[\rho_{\mathcal{R}}](t; c_{\text{ref}}) = \sum_{q=1}^{N_{\rho}} \eta_q \mathbf{\Lambda}_q(t; c_{\text{ref}}),$$

where $\Lambda_q(t; c_{\text{ref}})$ are $m \times m$ matrices with components

(4.5)
$$\Lambda_q^{(r,s)}(t;c_{\text{ref}}) = \int_0^t dt' \int_{\Omega_{\text{in}}} d\boldsymbol{x} \, \beta_q(\boldsymbol{x}) \widetilde{u}^{(s)}(t',\boldsymbol{x};c_{\text{ref}}) \partial_{t'} u^{(r)}(t',\boldsymbol{x};c_{\text{ref}}),$$

and $\widetilde{u}^{(s)}(t, \boldsymbol{x}; c_{\text{ref}})$ given by the interpolation of the estimated snapshots (3.31).

The regularization term in the objective function (2.28) can be chosen based on the prior information on c(x). For the simulations described in the next section we use either the TV norm of the wave speed or the squared Euclidean norm of η , i.e., Tikhonov regularization. We refer to Appendix E for the details on the regularization.

4.1. Regularization of the estimation of the internal wave. The computation of the estimated internal wave snapshots (3.31) involves the block Cholesky factor \mathbf{R} of the data driven Galerkin mass matrix, so we need to ensure that \mathbf{M} is symmetric and positive definite.

In the absence of noise, M is symmetric by reciprocity, but it may not be positive definite, especially if we over discretize in time, i.e., τ is too small, or if the separation between the sensors is much smaller than the central wavelength.

If data are noisy, let M_{noisy} be the mass matrix given by (3.25), and then set

$$\boldsymbol{M} = \frac{1}{2} \left(\boldsymbol{M}_{\text{noisy}} + \boldsymbol{M}_{\text{noisy}}^T \right),$$

to ensure the symmetry. In either case, if M is not positive definite, we regularize it by adding a small multiple of the block $M_{0,0}$ to the block diagonal. Since $M_{0,0} = D_0$ is computed in the known medium near the sensors, it is not affected by noise. Note that we use this particular regularization, as opposed to, say, spectral truncation, to ensure that we maintain the block Hankel plus Toeplitz algebraic structure of M seen from (3.25).

4.2. The inversion algorithm. The ROM and therefore the approximation of the internal wave are causal, so it is possible to carry out the inversion in a layer peeling fashion, by choosing a progressively larger end time T. Then, the inversion scheme would consist of two kinds of iterations: The outer iterations, which consider a progressively larger end time T, and the inner iterations that minimize the objective function for a given T. We describe next how we carry out the inner iterations. In our numerical simulations we used a single outer iteration, i.e., a fixed T.

There are two ways to carry out the inner iterations, called henceforth "approach 1" and "approach 2." The first approach updates $\tilde{\boldsymbol{u}}(t,\boldsymbol{x};c_{\text{ref}})$ while keeping $\partial_t \boldsymbol{u}(t,\boldsymbol{x};c_{\text{ref}})$ and the definition of $\rho(\boldsymbol{x})$ fixed, as given in the following algorithm.

(Inner iterations for approach 1)

Input: D_j for j = 0, ..., n-1, the Cholesky square root R of the mass matrix, and the initial guess $c_0(x)$ of the wave speed.

For $k \ge 1$ do

- 1. Set $c_{\text{ref}}(\boldsymbol{x}) = c_{k-1}(\boldsymbol{x})$ and compute $\boldsymbol{V}(\boldsymbol{x}; c_{\text{ref}})$.
- 2. Compute $\widetilde{u}^{(s)}(t, \boldsymbol{x}; c_{\text{ref}})$ using linear interpolation of $[\boldsymbol{V}(\boldsymbol{x}; c_{\text{ref}})\boldsymbol{R}\boldsymbol{e}_j]_s$, for time $t \in (0, \dots, (n-1)\tau)$, index $j = 0, \dots, n-1$ and $s = 1, \dots, m$.

3. Compute the $m \times m$ matrices $\{\mathbf{\Lambda}_q(t; c_{\text{ref}})\}_{q=1}^{N_{\rho}}$ defined componentwise by

$$\Lambda_q^{(r,s)}(t;c_{\mathrm{ref}}) = \int_0^t dt' \int_{\Omega_{\mathrm{in}}} d\boldsymbol{x} \, \beta_q(\boldsymbol{x}) \widetilde{u}^{(s)}(t',\boldsymbol{x};c_{\mathrm{ref}}) \partial_{t'} u^{(r)}(t',\boldsymbol{x};c_0)$$

for r, s = 1, ..., m and time t in the set $\{0, \tau, ..., (n-1)\tau\}$.

4. Determine the vector $\boldsymbol{\eta} = (\eta_1, \dots, \eta_{N_o})^T$ as the minimizer of the objective function

$$\sum_{j=0}^{n-1} \tau \left\| \boldsymbol{D}_j - \boldsymbol{D}_j(c_0) - \sum_{q=1}^{N_\rho} \eta_q \boldsymbol{\Lambda}_q(j\tau; c_{\text{ref}}) \right\|_F^2 + \text{ regularization}.$$

5. Compute $\widetilde{\rho}(\mathbf{x}) = \sum_{q=1}^{N_{\rho}} \eta_q \beta_q(\mathbf{x})$ and estimate the wave speed as

(4.6)
$$c_k(\mathbf{x}) = \frac{c_0(\mathbf{x})}{2} \left[\widetilde{\rho}(\mathbf{x}) + \sqrt{4 + \widetilde{\rho}^2(\mathbf{x})} \right].$$

6. Check for convergence and decide to continue or stop.

Output: The estimated wave speed.

In the second approach we change all the fields at each iteration. The algorithm is like the one above, with the following three exceptions:

1. At step 3, the matrices $\{\mathbf{\Lambda}_q(t;c_{\text{ref}})\}_{q=1}^{N_{\rho}}$ have the entries

$$\Lambda_q^{(r,s)}(t;c_{\text{ref}}) = \int_0^t dt' \int_{\Omega_{\text{in}}} d\boldsymbol{x} \, \beta_q(\boldsymbol{x}) \widetilde{u}^{(s)}(t',\boldsymbol{x};c_{\text{ref}}) \partial_{t'} u^{(r)}(t',\boldsymbol{x};c_{\text{ref}}).$$

- 2. At step 4, the objective function uses the recomputed data $D_j(c_{ref})$ at the current guess of the wave speed, instead of $D_j(c_0)$.
- 3. At step 5, the wave speed is estimated by

(4.7)
$$c_k(\mathbf{x}) = \frac{c_{\text{ref}}(\mathbf{x})}{2} \left[\widetilde{\rho}(\mathbf{x}) + \sqrt{4 + \widetilde{\rho}^2(\mathbf{x})} \right].$$

Here is the motivation for both approaches: If in the definition of $\{\Lambda_q(t; c_{\text{ref}})\}_{q=1}^{N_\rho}$ we had the true internal wave $\boldsymbol{u}(t, \boldsymbol{x})$ instead of $\widetilde{\boldsymbol{u}}(t, \boldsymbol{x}; c_{\text{ref}})$, then not counting the regularization, the problem would be a linear least squares problem that can be solved in one iteration. As explained in section 3.2, the snapshots of the true wave differ from our estimates only because we replace the unknown $\boldsymbol{V}(\boldsymbol{x})$ by the computable $\boldsymbol{V}(\boldsymbol{x}; c_{\text{ref}})$. The idea of the first approach is to correct $\boldsymbol{V}(\boldsymbol{x}; c_{\text{ref}})$ as we iterate, hoping that it gets closer to $\boldsymbol{V}(\boldsymbol{x})$. The other fields remain equal to their initial values.

The second approach is basically the Gauss–Newton method for minimizing the objective function. Since all the fields are updated at each iteration, it may look like it involves more computations. However, since both approaches need the orthonormal basis stored in $V(x; c_{ref})$, whose computation involves the calculation of the reference snapshots, there is no

extra computational cost. Moreover, this second approach performs better in the numerical simulations, as shown in the next section.

We end the section with a brief comparison of the computational cost per iteration of our algorithms and of FWI. They all require the solution of the forward problem. In FWI, the Jacobian of the objective function is typically computed using an adjoint method [27]. Its cost is comparable to that of computing the matrices $\{\Lambda_q(t; c_{\text{ref}})\}_{q=1}^{N_\rho}$ at step 3 of our algorithms. The overhead in our algorithms is due to the block Cholesky factorization of the mass matrix. This is $\mathcal{O}(m^3n^3)$, and it is small compared to the computation of the Jacobian of the objective functions. Note that $V(x; c_{\text{ref}})$ does not need to fit in computational memory. One can partition the imaging domain into sections and compute it for each section separately.

5. Numerical results. In this section we present numerical results in a two dimensional rectangular domain Ω , with one side close and parallel to the array, modeled as the sound hard boundary $\partial\Omega_N$. The other three sides are modeled as the sound soft boundary $\partial\Omega_D$. Two of them are perpendicular to the array and are close enough to affect the waves over the duration $2(n-1)\tau$ of the data gather. The remaining side is far away from the array and plays no role. The sketch in Figure 2.1 illustrates the setup.

The probing pulse is the Gaussian

(5.1)
$$f(t) = \frac{2\pi}{\sqrt{2}} \exp\left(-\frac{B^2 t^2}{2}\right) \cos(\omega_c t),$$

modulated with the cosine at central frequency $\omega_c/(2\pi)$ and with bandwidth determined by $B = \omega_c/4$. After the "pulse compression" we get

(5.2)
$$F(t) = f(-t) \star f(t) = \frac{\pi^{5/2}}{B} \exp\left(-\frac{B^2 t^2}{4}\right) \left[\cos(\omega_c t) + \exp\left(-\frac{\omega_c^2}{B^2}\right)\right]$$
$$\approx \frac{\pi^{5/2}}{B} \exp\left(-\frac{B^2 t^2}{4}\right) \cos(\omega_c t).$$

This does not have finite support, but it is negligible for $|t| \ge 2\sqrt{3}/B$, so the theory applies with $t_F = 2\sqrt{3}/B$.

We refer to Appendix E for the details on the calculation of the objective function and its minimization. Here we give the numerical results obtained with the two approaches described above and also with the traditional FWI method, which differs from approach 2 by the approximation of the internal wave. Instead of the estimate (3.31), FWI uses the wave in the reference medium.

In all the figures, we scale the wave speed by the constant value \bar{c} near the array, and the lengths by the central wavelength $\lambda_c = 2\pi \bar{c}/\omega_c$. Following the typical terminology in array imaging, we mean by "range" the direction orthogonal to the array and by "cross-range" the direction along the array. The time sampling step τ , the number n of time instants, the number m of sensors, and the separation between them vary among the experiments and are specified in the two sections below.

5.1. Test case 1. The first set of results is for the medium shown in Figure 5.1. The array consists of m = 40 sensors, spaced at distance $\lambda_c/4$ apart. The time sampling step is

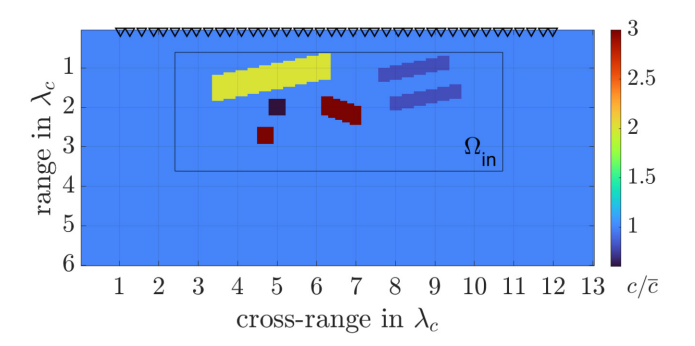


Figure 5.1. The wave speed in the first test medium. The colorbar shows the variations of $c(\mathbf{x})/\bar{c}$. The 40 sensors in the array are shown with the triangles at the top of the domain. The boundary of the rectangular inversion domain $\Omega_{\rm in}$ is shown with the black line.

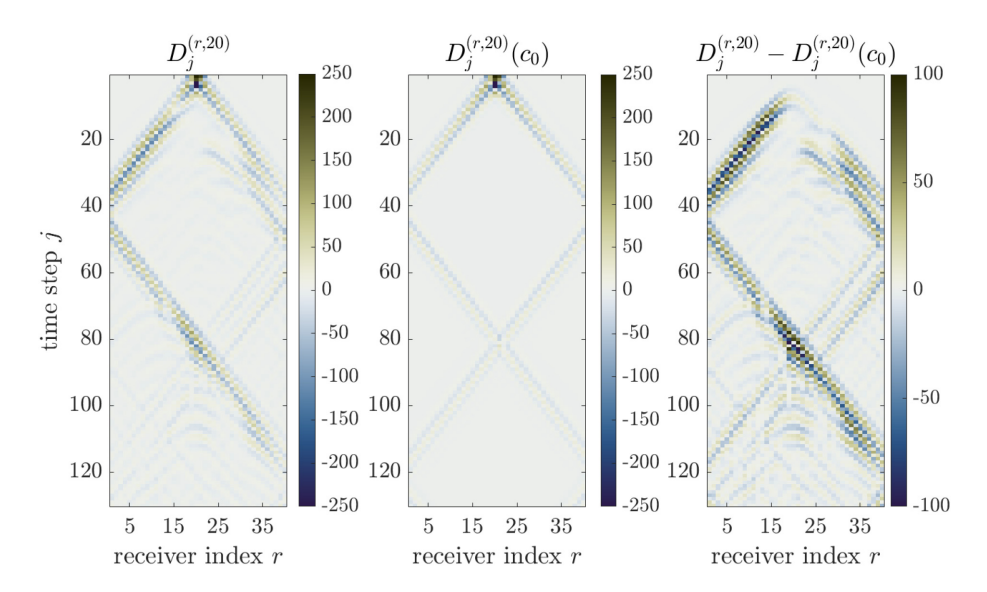


Figure 5.2. The $20^{\rm th}$ column of the data matrices, displayed as a function of the receiver index in the abscissa and time index in the ordinate. The magnitude of the entries is given in the colorbar.

 $\tau = \pi/(3\omega_c)$ and n = 75. The mass matrix \boldsymbol{M} is regularized as explained in section 4.1, by adding the 0.01 multiple of $\boldsymbol{M}_{0,0}$ to the block diagonal.

We display in the left plot of Figure 5.2 one column of the data matrix D(t), corresponding to the central source excitation, indexed by s = 20. Its analogue $\{D^{(r,20)}(t;c_0)\}_{r=1}^{40}$, computed with the initial guess $c_0(x) = \bar{c}$ of the wave speed, is shown in the middle plot. It contains just the echoes from the side boundaries. The echoes from the unknown inclusions are prominent in the right plot, which displays the difference $\{D^{(r,20)}(t) - D^{(r,20)}(t;c_0)\}_{r=1}^{40}$.

As explained in the previous section, the essential difference between the ROM based inversion and FWI is the estimation of the internal wave. Figure 5.3 shows the estimates for the point \boldsymbol{x} indicated with a black cross in the top plot. The true internal wave $\boldsymbol{u}_j(\boldsymbol{x}) = \boldsymbol{V}(\boldsymbol{x})\boldsymbol{R}\boldsymbol{e}_j$, which cannot be computed from the data set and requires knowing $c(\boldsymbol{x})$, is shown in the left plot in the middle line. The initial FWI estimate $\boldsymbol{u}_j(\boldsymbol{x};c_0) = \boldsymbol{V}(\boldsymbol{x};c_0)\boldsymbol{R}(c_0)\boldsymbol{e}_j$ is shown in the right plot in the middle line, and the ROM estimate $\tilde{\boldsymbol{u}}_j(\boldsymbol{x};c_0) = \boldsymbol{V}(\boldsymbol{x};c_0)\boldsymbol{R}\boldsymbol{e}_j$ is

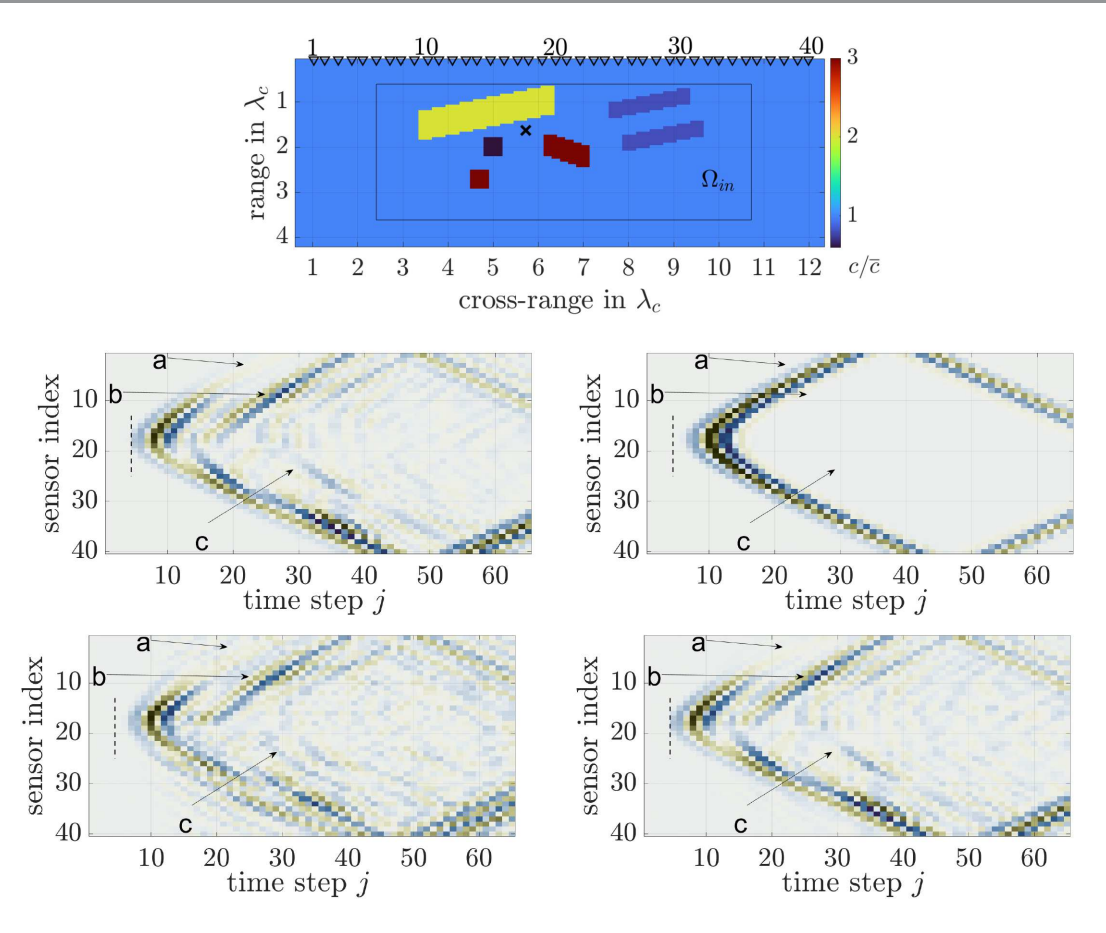


Figure 5.3. Top: The medium and the point \boldsymbol{x} at which we estimate the internal solution, indicated with a cross. Middle left: The true internal wave $\boldsymbol{u}_j(\boldsymbol{x}) = \{u^{(s)}(j\tau,\boldsymbol{x})\}_{s=1}^{40}$. Middle right: The initial FWI estimate $\boldsymbol{u}_j(\boldsymbol{x};c_0) = \{u^{(s)}(j\tau,\boldsymbol{x};c_0)\}_{s=1}^{40}$ of the internal wave. Bottom left: The initial ROM estimate $\widetilde{\boldsymbol{u}}_j(\boldsymbol{x};c_0) = \{\widetilde{u}^{(s)}(j\tau,\boldsymbol{x};c_0)\}_{s=1}^{40}$ of the internal wave. Bottom right: The final ROM estimate of the internal wave.

shown in the bottom left plot. To compare the FWI and ROM initial estimates, we identify in the true internal wave three arrival events: The first is the direct arrival, indicated by the arrow a, which is the wave that travels from the array to x, through the top fast inclusion. The dashed line marks the travel time from the closest source to x. The other two events, indicated by the arrows b and c, are waves scattered multiple times between the inclusions and the top boundary. Note that both the ROM and FWI estimates contain the direct arrival, although it lies behind the dashed line by about 2τ , due to the incorrect kinematics given by $c_0(x)$. The FWI estimate does not account for the multiply scattered arrival events, as it uses no information about the true medium. The ROM estimate is superior, because it contains these events, although they are slightly displaced, due to the wrong kinematics. The ROM based inversion corrects the kinematics as we iterate, and the final estimate of the internal wave, shown in the bottom right plot, is very close to the uncomputable true internal wave.

The inversion results are shown in Figure 5.4. They are obtained with the parametrization (4.3), using the "hat basis" $\{\beta_j(\boldsymbol{x})\}_{j=1}^{N_\rho}$, defined on a uniform mesh in $\Omega_{\rm in}$, with spacing $3\lambda_c/16$

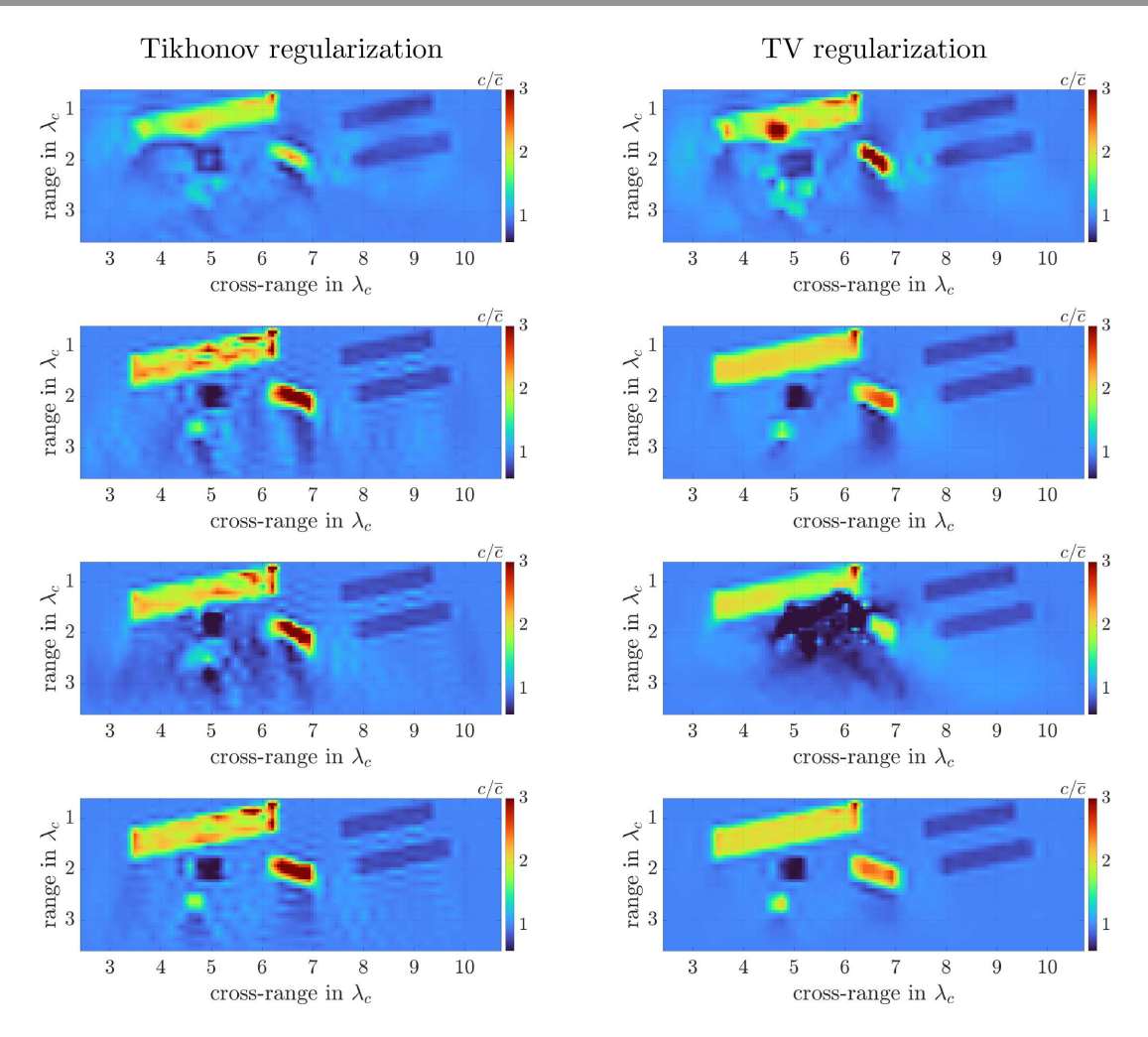


Figure 5.4. Inversion results for the setup shown in Figure 5.1. We display the results in the subdomain Ω_{in} . The left column shows the results for Tikhonov regularization and the right column for TV regularization. From top to bottom, the first row is for approach 1, the second row is for approach 2, and the third row is for FWI. The last row shows the ideal inversion results, obtained with the true internal wave. The colorbar is kept the same as in Figure 5.1.

in range and $\lambda_c/4$ in cross-range. Each function $\beta_j(\mathbf{x})$ is piecewise linear on the mesh, equal to one at the jth mesh point, and zero at all other points. We use the two regularization methods mentioned in the previous section: Tikhonov, which penalizes the squared Euclidean norm of the vector $\boldsymbol{\eta}$ of coefficients in (4.3) (left plots), and TV, which penalizes the $L^1(\Omega_{\rm in})$ norm of the gradient of the wave speed (right plots). The details of the regularization, and the regularization parameters, are given in Appendix E.

To assess the quality of the inversion, we display in the bottom row of Figure 5.4 the ideal result, obtained with the true internal wave u(t, x), which cannot be computed without knowing the medium. Were it not for the regularization, this ideal result could be obtained in a single step. However, since we penalize the changes of $\rho(x)$ and therefore of c(x), we need a

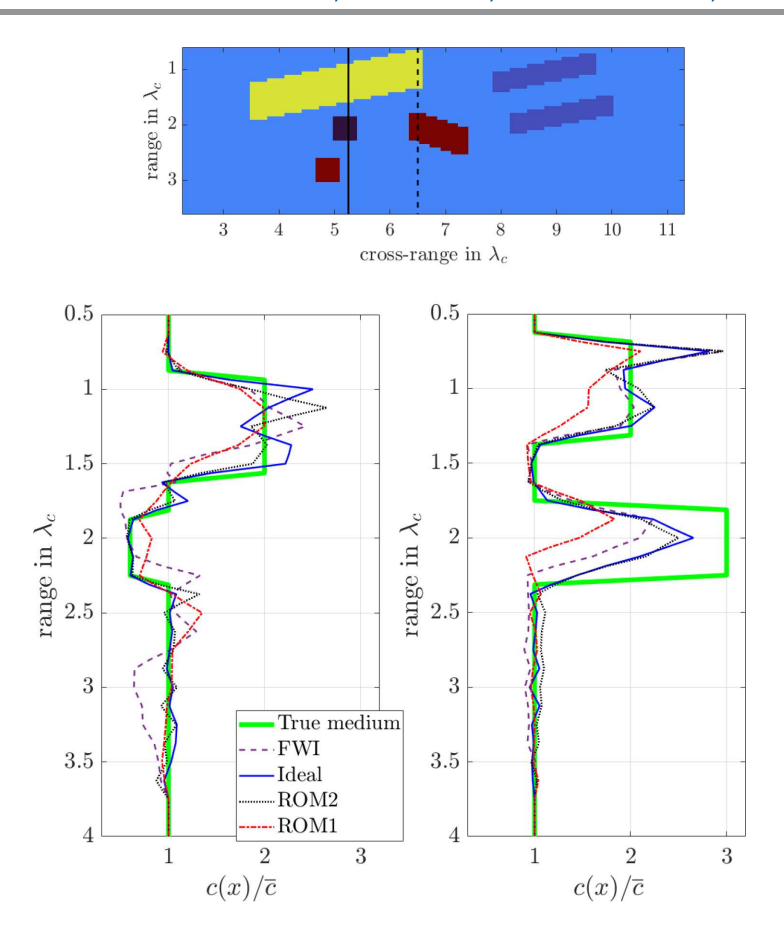


Figure 5.5. Two cross-sections of the inversion results, indicated in the top plot by the solid and dotted vertical lines.

few steps to reach convergence. The ROM approach 2 gives a result that is close to the ideal one, as seen from the plots shown in the second line. The ROM approach 1 result, shown in the first line, is not as good. In particular, the bottom inclusion is not correctly identified and the values of the wave speed in the other inclusions are not as close as those given by approach 2. The FWI results are shown in the third line. They are better for Tikhonov regularization, but the bottom inclusion is misplaced due to the wrong kinematics of the inclusions above it. For the TV regularization, the FWI method gets stuck in a local minimum, and thus it cannot identify the bottom two inclusions.

Figure 5.5 shows two cross-sections of the images, where the misplacement of the bottom inclusions by FWI and approach 1 are more evident. We also show in Figure 5.6 the relative data misfit: $\left[(\sum_{j=0}^{2n-1} \| \boldsymbol{D}_j - \boldsymbol{D}_j(c_k) \|_F^2) / (\sum_{j=0}^{2n-1} \| \boldsymbol{D}_j \|_F^2) \right]^{\frac{1}{2}}$, where $c_k(\boldsymbol{x})$ is the estimated wave speed at the kth iteration. This misfit cannot be zero even in the ideal inversion, because the unknown $c(\boldsymbol{x})$ cannot be represented exactly in the hat basis and because we use regularization. Note that approach 2 achieves the ideal fit, while the other methods give a worse fit. This is consistent with the results in Figure 5.4.

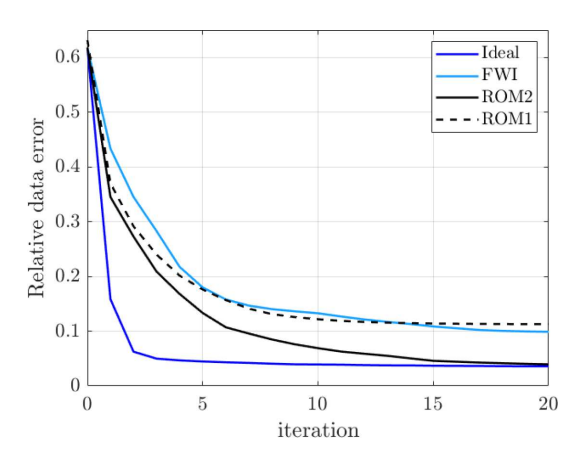


Figure 5.6. Data fit of the inversion methods.

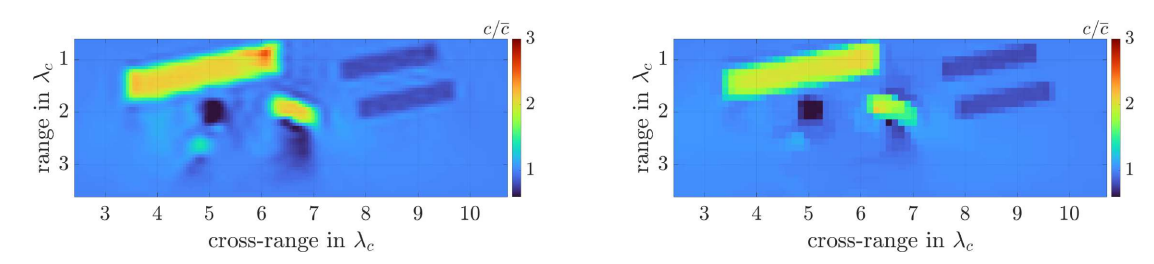


Figure 5.7. The stability of the inversion algorithm with respect to changes of the basis in the parametrization of $\rho(\mathbf{x})$. Both results are obtained with TV regularization. The left plot is for the Gaussian basis and the right plot is for the pixel basis.

We now focus attention on the better approach 2, and illustrate in Figure 5.7 its stability to the change of basis $\{\beta_j(\boldsymbol{x})\}_{j=1}^{N_\rho}$ of the search space \mathcal{R} : The left plot uses a Gaussian basis, where $\beta_j(\boldsymbol{x})$ peaks at the jth mesh point, and has the standard deviation $0.0796\lambda_c$ in range and $0.11\lambda_c$ in cross-range. The mesh is the same as for the basis of hat functions and the standard deviations are chosen so that the Gaussian functions have the same full width at half maximum as the hat functions [1]. The right plot is for a pixel basis defined on a uniform, square mesh with spacing $\lambda_c/8$, where $\beta_j(\boldsymbol{x})$ equals one in the jth grid cell and zero elsewhere. Both results are obtained with TV regularization. It may appear natural to use the pixel basis in conjunction with TV regularization to recover a piecewise constant wave speed. However, the jump discontinuities introduced by this basis cause spurious scattering events, because the unknown inclusions are misaligned with the inversion mesh. Consequently, the image is slightly worse and, in particular, the bottom small inclusion is barely seen. The continuous basis functions, like the hats and the Gaussians, are not so sensitive to the mesh misalignment and give a better result.

The robustness of approach 2 to 10% additive noise is illustrated in Figure 5.8. To mitigate the noise, we regularized the mass matrix as explained in section 4.1, by adding the multiple 0.87 of $M_{0,0}$ to the block diagonal. We display the inversion results obtained with Tikhonov regularization (left plot) and TV regularization (right plot). We use the same basis of hat functions as in Figure 5.4, and the noise model is as follows: For j = 1, ..., 2n-1, we add to D_j

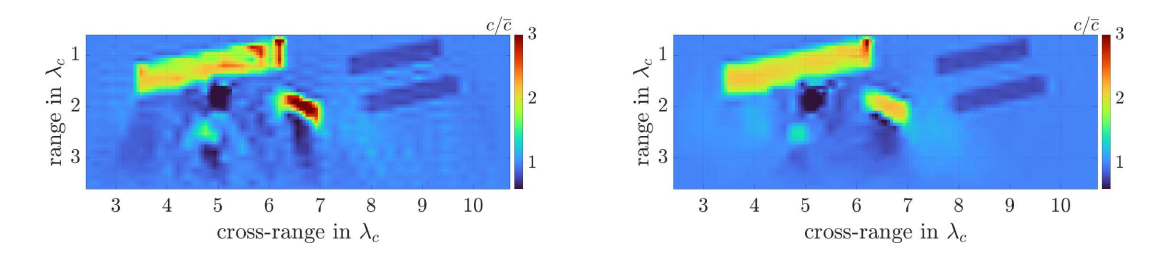


Figure 5.8. Inversion results using data contaminated with 10% noise. Left plot: Tikhonov regularization. Right plot: TV regularization.

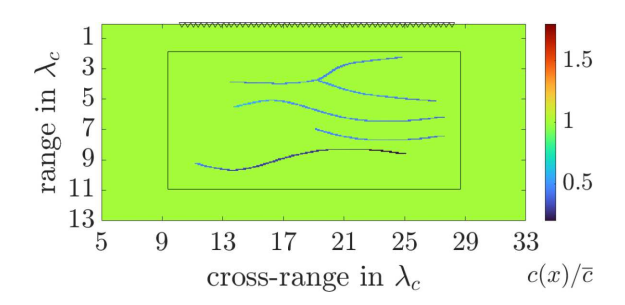


Figure 5.9. The wave speed in the second test medium, with thin, fracture like, slow inhomogeneities. The colorbar shows the variations of $c(\mathbf{x})/\bar{c}$. The 50 sensors in the array are shown with the triangles at the top of the domain.

the matrix \mathfrak{N}_j , with m^2 entries $(\mathfrak{N}^{(r,s)})_{r,s=1}^m$ that are independent and identically distributed Gaussian random variables, with mean zero and variance $\frac{0.1^2}{2nm^2}\sum_{j=0}^{2n-1}\|\boldsymbol{D}_j\|_F^2$.

5.2. Test case 2. The second set of results is for the medium shown in Figure 5.9, with four thin and slow inhomogeneities, which model fractures. The array has m = 50 sensors, at distance $0.35\lambda_c$ apart, the time step is $\tau = \pi/(3\omega_c)$, and n = 118.

The main difference between this test case and the one considered in the previous section is that $c_0(\boldsymbol{x}) = \bar{c}$ gives a good approximation of the kinematics, which is only slightly perturbed by the thin inhomogeneities. This is why our initial estimate $\tilde{u}(t, \boldsymbol{x}; c_0)$ of the internal wave is close to the true wave $\boldsymbol{u}(t, \boldsymbol{x})$, as illustrated in Figure 5.10, for the point \boldsymbol{x} marked with the red cross in the left plot. Note how the estimate contains the marked 4 arrivals in the middle plot. The arrival marked by d is for the wave scattered once at the bottom inhomogeneity. The events marked with c and b are surface multiples, which scattered at the sound hard boundary and the top inhomogeneity. The later arrival marked a is also correctly identified.

In Figure 5.11 we compare the inversion results given by the ROM approach 2 and FWI. We parametrize $\rho(x)$ with the hat basis, on a grid with steps $3\lambda_c/16$ in range and $5\lambda_c/16$ in cross-range. We use TV regularization, with the regularization parameter given in Appendix E. Since the initial estimate of the internal wave is so accurate, the ROM approach 2 identifies the four thin inhomogeneities at the first step. The remaining four iterations sharpen slightly the image. FWI gives a spurious feature at the first iteration, because it uses the inaccurate estimate $u(t, x; c_0)$ of the internal wave. This spurious feature disappears at the 5th iteration, but the lower inhomogeneities are not reconstructed. The optimization is stuck in a local minimum and the result does not improve if we iterate more.

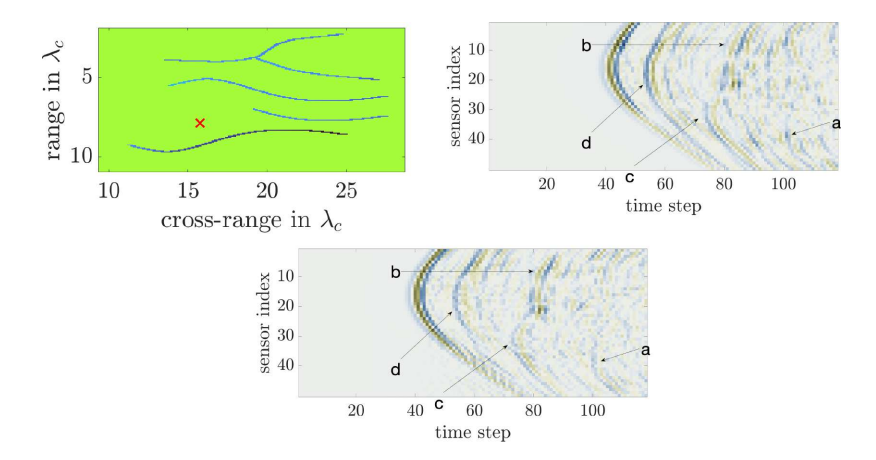


Figure 5.10. The internal wave at the point x marked with the red cross in the left plot. Middle plot displays the true internal wave. The right plot is our initial estimate of this wave.

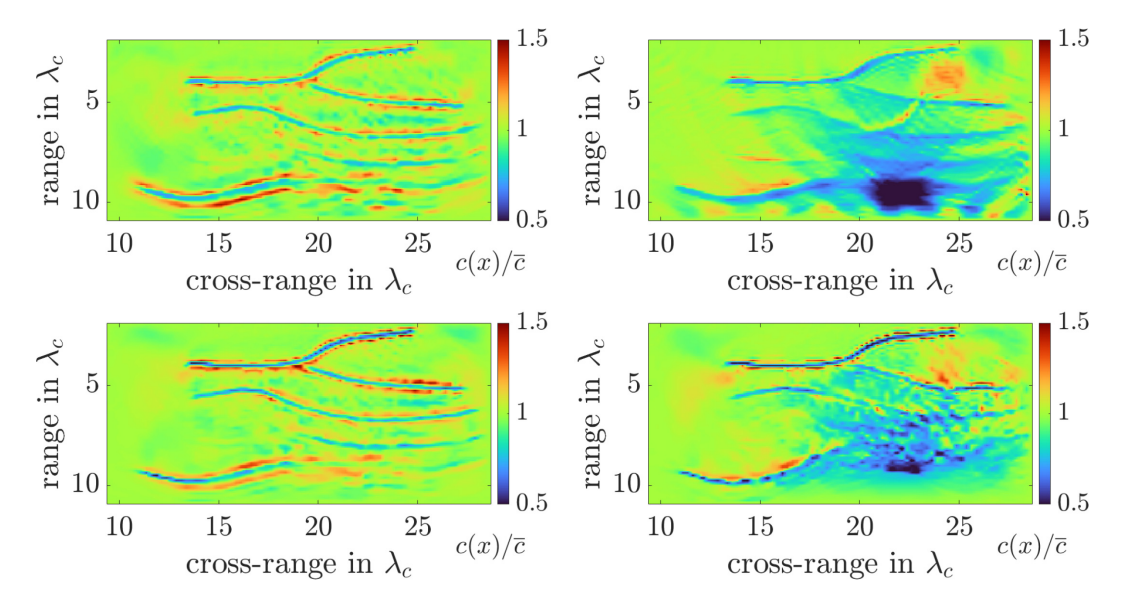


Figure 5.11. Inversion results: Top row shows the first iteration. Bottom row shows the fifth iteration. The left column is for the ROM approach 2 and the right column is for FWI.

6. Summary. We introduced a novel waveform inversion methodology that estimates the wave speed in the acoustic wave equation from the time resolved response matrix gathered by an array of sensors that emit probing pulses and measure the generated wave. The algorithm uses a least squares data fit formulation of the problem, where the forward map from the wave speed to the data is defined using the Lippmann–Schwinger integral equation for the scattered wave field. This map is nonlinear and, typically, the least squares objective function has multiple local minima that are far from the true wave speed. This behavior is known to be caused by the following factors: (1) the data acquisition geometry, i.e., the array measures the backscattered waves but not the waves transmitted through the unknown medium; (2) the multiple scattering of the waves on the rough part of the medium, called the reflectivity, and modeled, for example, by the jump discontinuities of the wave speed; and (3) the cycle

skipping phenomenon, caused by kinematic errors that exceed half a period of the probing waves. Kinematics refers to the smooth part of the wave speed, which determines the travel times of the waves, and cycle skipping is especially problematic for high frequency waves.

The novelty of our methodology is that these effects can be mitigated partially using a data driven estimate of the internal wave, i.e., the wave field at points inside the inaccessible medium. Full knowledge of this wave would linearize the forward map and thus turn the problem into an easier, linear least squares minimization. Our estimate is an approximation of the internal wave that is more accurate than the usual ones used in iterative optimization methods. In particular, we prove that it satisfies automatically the measured data.

Our estimate of the internal wave is rooted in a data driven ROM of the wave propagator operator, which controls the evolution of the wave field at discrete time instants separated by an appropriately chosen interval. The computation of the estimate of the internal wave is cost effective and it is robust to additive noise. The accuracy of the estimate depends mostly on the guess kinematics and not the reflectivity, and it can be improved iteratively. We introduced an inversion algorithm based on the estimated internal wave and assessed its performance with numerical simulations.

Appendix A. Derivation of the expression (2.19). This derivation can also be found in [8]. We repeat it here for the convenience of the reader. We begin by writing the solution of (2.7)–(2.8) as

(A.1)
$$P^{(s)}(t, \boldsymbol{x}) = F(t) \star_t G(t, \boldsymbol{x}, \boldsymbol{x}_s),$$

where $G(t, \boldsymbol{x}, \boldsymbol{x}_s)$ is the causal Green's function, satisfying

(A.2)
$$\left[\partial_t^2 + A(c)\right] G(t, \boldsymbol{x}, \boldsymbol{x}_s) = \delta'(t) \delta_{\boldsymbol{x}_s}(\boldsymbol{x}), \qquad t \in \mathbb{R}, \ \boldsymbol{x} \in \Omega,$$

(A.2)
$$\left[\partial_t^2 + A(c) \right] G(t, \boldsymbol{x}, \boldsymbol{x}_s) = \delta'(t) \delta_{\boldsymbol{x}_s}(\boldsymbol{x}), \qquad t \in \mathbb{R}, \ \boldsymbol{x} \in \Omega,$$
(A.3)
$$G(t, \boldsymbol{x}, \boldsymbol{x}_s) \equiv 0, \qquad t < 0, \ \boldsymbol{x} \in \Omega,$$

(A.4)
$$[1_{\partial\Omega_{D}}(\boldsymbol{x}) + 1_{\partial\Omega_{N}}(\boldsymbol{x})\partial_{n}] G(t,\boldsymbol{x},\boldsymbol{x}_{s}) = 0, \qquad t \in \mathbb{R}, \ \boldsymbol{x} \in \partial\Omega.$$

This problem can be solved using separation of variables: Expanding $G(t, \mathbf{x}, \mathbf{x}_s)$ in the orthonormal basis given by the eigenfunctions $\{y_j(x)\}_{j\geq 1}$ of A(c), and imposing the jump conditions at t=0, due to the derivative of the Dirac $\delta(t)$ in (A.2), we get

$$(A.5) G(t, \boldsymbol{x}, \boldsymbol{x}_s) = H(t) \cos\left[t\sqrt{A(c)}\right] \delta_{\boldsymbol{x}_s}(\boldsymbol{x}) = H(t) \sum_{j=1}^{\infty} \cos(t\sqrt{\theta_j}) y_j(\boldsymbol{x}) y_j(\boldsymbol{x}_s),$$

where H(t) is the Heaviside step function, equal to 1 at t > 0 and 0 otherwise. Therefore, (A.1) becomes³

(A.6)
$$P^{(s)}(t, \boldsymbol{x}) = F(t) \star_t H(t) \sum_{j=1}^{\infty} \cos(t\sqrt{\theta_j}) y_j(\boldsymbol{x}) y_j(\boldsymbol{x}_s)$$
$$= \sum_{j=1}^{\infty} \left[F(t) \star_t H(t) \cos(t\sqrt{\theta_j}) \right] y_j(\boldsymbol{x}) y_j(\boldsymbol{x}_s).$$

³Because the series (A.5) converges pointwise in t, and the partial sums are dominated by an integrable function in t, we could move the time convolution inside the series using the dominated convergence theorem.

We can evaluate the convolution in (A.6) using the Fourier transform formula

$$\int_{-\infty}^{\infty} dt \, H(t) \cos(t\sqrt{\theta_j}) e^{i\omega t} = \frac{\pi}{2} \left[\delta(\omega - \sqrt{\theta_j}) + \delta(\omega + \sqrt{\theta_j}) \right] + \frac{i\omega}{\theta_j - \omega^2}$$

and obtain

$$F(t) \star_t H(t) \cos(t\sqrt{\theta_j}) = \frac{1}{4} \left[\widehat{F}(\sqrt{\theta_j}) e^{-it\sqrt{\theta_j}} + \widehat{F}(-\sqrt{\theta_j}) e^{it\sqrt{\theta_j}} \right]$$
$$+ \int_{-\infty}^{\infty} \frac{d\omega}{2\pi} \frac{i\omega \widehat{F}(\omega)}{(\theta_j - \omega^2)} e^{-i\omega t},$$

where the first term simplifies because by the definition of F(t) and the fact that the probing pulse is real valued, we have $\widehat{F}(\omega) = \widehat{F}(-\omega)$, for all $\omega \in \mathbb{R}$. Therefore,

$$F(t) \star_t H(t) \cos(t\sqrt{\theta_j}) = \frac{1}{2} \widehat{F}(\sqrt{\theta_j}) \cos(t\sqrt{\theta_j}) + \int_{-\infty}^{\infty} \frac{d\omega}{2\pi} \frac{i\omega \widehat{F}(\omega)}{(\theta_j - \omega^2)} e^{-i\omega t},$$

and substituting in (A.6) and recalling the definition (2.11) of the even wave, we get

$$W^{(s)}(t, \boldsymbol{x}) = \sum_{j=1}^{\infty} \left[\widehat{F}(\sqrt{\theta_j}) \cos(t\sqrt{\theta_j}) + \int_{-\infty}^{\infty} \frac{d\omega}{\pi} \frac{i\omega \widehat{F}(\omega) \cos(\omega t)}{(\theta_j - \omega^2)} \right] y_j(\boldsymbol{x}) y_j(\boldsymbol{x}_s).$$

The integral vanishes, because the integrand is odd, and the result becomes

$$W^{(s)}(t, \boldsymbol{x}) = \sum_{j=1}^{\infty} \widehat{F}(\sqrt{\theta_j}) \cos(t\sqrt{\theta_j} t) y_j(\boldsymbol{x}) y_j(\boldsymbol{x}_s)$$
$$= \cos[t\sqrt{A(c)}] \widehat{F}[\sqrt{A(c)}] \delta_{\boldsymbol{x}_s}(\boldsymbol{x}).$$

This is (2.19), by definition (2.16). That $W^{(s)}(t, x)$ solves the initial boundary value problem (2.12)–(2.15) is obvious from this expression.

Appendix B. Proof of Proposition 2.2. Let us undo the similarity transformation in (2.6) and work for the moment with the causal wave

(B.1)
$$w^{(s)}(t, \mathbf{x}) = H(t)c(\mathbf{x})W^{(s)}(t, \mathbf{x}),$$

defined for $t \in \mathbb{R}$. We deduce from (2.12)–(2.14) that this satisfies

(B.2)
$$\left[\partial_t^2 - c^2(\boldsymbol{x}) \Delta \right] w^{(s)}(t, \boldsymbol{x}) = \delta'(t) \bar{c} \varphi^{(s)}(\boldsymbol{x}), \qquad t \in \mathbb{R}, \ \boldsymbol{x} \in \Omega,$$
(B.3)
$$w^{(s)}(t, \boldsymbol{x}) \equiv 0, \qquad t < 0, \ \boldsymbol{x} \in \Omega,$$

$$(\mathrm{B.3}) \hspace{1cm} w^{(s)}(t,\boldsymbol{x}) \equiv 0, \hspace{1cm} t < 0, \ \boldsymbol{x} \in \Omega,$$

(B.4)
$$[1_{\partial\Omega_D}(\boldsymbol{x}) + 1_{\partial\Omega_N}(\boldsymbol{x})\partial_n] w^{(s)}(t,\boldsymbol{x}) = 0, \qquad t \in \mathbb{R}, \ \boldsymbol{x} \in \partial\Omega,$$

where we used the jump conditions for the derivative of the Dirac $\delta(t)$, which give

$$\bar{c}\varphi^{(s)}(\boldsymbol{x}) = \lim_{\varepsilon \searrow 0} \left[w^{(s)}(\varepsilon, \boldsymbol{x}) - w^{(s)}(-\varepsilon, \boldsymbol{x}) \right] = w^{(s)}(0+, \boldsymbol{x}),$$

$$0 = \lim_{\varepsilon \searrow 0} \left[\partial_t w^{(s)}(\varepsilon, \boldsymbol{x}) - \partial_t w^{(s)}(-\varepsilon, \boldsymbol{x}) \right] = \partial_t w^{(s)}(0+, \boldsymbol{x}).$$

Similarly, we define the reference wave

(B.5)
$$w^{(s)}(t, \mathbf{x}; c_{\text{ref}}) = H(t)c_{\text{ref}}(\mathbf{x})W^{(s)}(t, \mathbf{x}; c_{\text{ref}}),$$

which solves the analogue of (B.2)–(B.4), with $c(\boldsymbol{x})$ replaced by $c_{\text{ref}}(\boldsymbol{x})$. Then, the "scattered wave"

(B.6)
$$w_{sc}^{(s)}(t, \mathbf{x}) = w^{(s)}(t, \mathbf{x}) - w^{(s)}(t, \mathbf{x}; c_{ref})$$

satisfies the equation,

(B.7)
$$\left[\partial_t^2 - c_{\text{ref}}^2(\boldsymbol{x}) \Delta \right] w_{\text{sc}}^{(s)}(t, \boldsymbol{x}) = \frac{\left[c^2(\boldsymbol{x}) - c_{\text{ref}}^2(\boldsymbol{x}) \right]}{c^2(\boldsymbol{x})} \partial_t^2 w^{(s)}(t, \boldsymbol{x}), \quad t \in \mathbb{R}, \ \boldsymbol{x} \in \Omega,$$

driven by the unknown variations of the wave speed, and can be written via the principle of linear superposition in terms of the Green's function $\mathcal{G}(t, \boldsymbol{x}, \boldsymbol{x}'; c_{\text{ref}})$ for the wave operator in the reference medium. This is the solution of

(B.8)
$$\left[\frac{1}{c_{\text{ref}}^2(\boldsymbol{x})}\partial_t^2 - \Delta\right] \mathcal{G}(t, \boldsymbol{x}, \boldsymbol{x}'; c_{\text{ref}}) = \delta(t)\delta_{\boldsymbol{x}'}(\boldsymbol{x}), \qquad t \in \mathbb{R}, \ \boldsymbol{x} \in \Omega$$

(B.9)
$$\mathcal{G}(t, \boldsymbol{x}, \boldsymbol{x}'; c_{\text{ref}}) \equiv 0, \qquad t < 0, \ \boldsymbol{x} \in \Omega,$$

(B.10)
$$[1_{\partial\Omega_{D}}(\boldsymbol{x}) + 1_{\partial\Omega_{N}}(\boldsymbol{x})\partial_{n}] \mathcal{G}(t,\boldsymbol{x},\boldsymbol{x}';c_{\text{ref}}) \equiv 0, \qquad t \in \mathbb{R}, \ \boldsymbol{x} \in \partial\Omega$$

and it is related to the Green's function $G(t, \boldsymbol{x}, \boldsymbol{x}'; c_{\text{ref}})$ in Proposition 2.2 by

(B.11)
$$\partial_t \mathcal{G}(t, \boldsymbol{x}, \boldsymbol{x}'; c_{\text{ref}}) = c_{\text{ref}}(\boldsymbol{x}) c_{\text{ref}}(\boldsymbol{x}') G(t, \boldsymbol{x}, \boldsymbol{x}'; c_{\text{ref}}).$$

The principle of linear superposition gives

$$w_{\rm sc}^{(s)}(t, \boldsymbol{x}) = \int_{-\infty}^{\infty} dt' \int_{\Omega} d\boldsymbol{x}' \, \frac{[c^2(\boldsymbol{x}') - c_{\rm ref}^2(\boldsymbol{x}')]}{c^2(\boldsymbol{x}')c_{\rm ref}^2(\boldsymbol{x}')} \partial_{t'}^2 w^{(s)}(t', \boldsymbol{x}') \mathcal{G}(t - t', \boldsymbol{x}, \boldsymbol{x}'; c_{\rm ref}),$$

and after one step of integration by parts in t', we get

$$w_{\rm sc}^{(s)}(t, \boldsymbol{x}) = -\int_{-\infty}^{\infty} dt' \int_{\Omega} d\boldsymbol{x}' \frac{[c^2(\boldsymbol{x}') - c_{\rm ref}^2(\boldsymbol{x}')]}{c^2(\boldsymbol{x}')c_{\rm ref}^2(\boldsymbol{x}')} \partial_{t'} w^{(s)}(t', \boldsymbol{x}') \partial_{t'} \mathcal{G}(t - t', \boldsymbol{x}, \boldsymbol{x}'; c_{\rm ref}).$$

Substituting

$$\begin{aligned} \partial_{t'} \mathcal{G}(t - t', \boldsymbol{x}, \boldsymbol{x}'; c_{\text{ref}}) &= -\partial_{t} \mathcal{G}(t - t', \boldsymbol{x}, \boldsymbol{x}'; c_{\text{ref}}) \\ &= -c_{\text{ref}}(\boldsymbol{x}) c_{\text{ref}}(\boldsymbol{x}') G(t - t', \boldsymbol{x}, \boldsymbol{x}'; c_{\text{ref}}) \end{aligned}$$

into this equation, using definitions (B.1) and (B.6), and recalling that $G(t - t', \boldsymbol{x}, \boldsymbol{x}'; c_{\text{ref}})$ vanishes at t < t', we get

$$\frac{c(\boldsymbol{x})}{c_{\text{ref}}(\boldsymbol{x})}W^{(s)}(t,\boldsymbol{x}) - W^{(s)}(t,\boldsymbol{x};c_{\text{ref}}) = \int_0^t dt' \int_{\Omega} d\boldsymbol{x}' \frac{[c^2(\boldsymbol{x}') - c_{\text{ref}}^2(\boldsymbol{x}')]}{c(\boldsymbol{x}')c_{\text{ref}}(\boldsymbol{x}')} \partial_{t'}W^{(s)}(t',\boldsymbol{x}') \times G(t-t',\boldsymbol{x},\boldsymbol{x}';c_{\text{ref}})$$

for t > 0. The result of the proposition follows from this equation evaluated at $\mathbf{x} = \mathbf{x}_r$, because $c(\mathbf{x}_r) = c_{\text{ref}}(\mathbf{x}_r) = \bar{c}$.

Appendix C. Derivation of (3.1). Recall from section 2.2 the spectral decomposition of the operator A(c), and the definition of functions of this operator. We have from (2.19), definitions (3.2), (3.4), and the fact that functions of A(c) commute that

(C.1)
$$W^{(s)}(t, \boldsymbol{x}) = \widehat{\mathfrak{f}}[\sqrt{A(c)}] \cos[t\sqrt{A(c)}] u_0^{(s)}(\boldsymbol{x})$$

$$= \sum_{j=1}^{\infty} \widehat{\mathfrak{f}}(\sqrt{\theta_j}) \cos(t\sqrt{\theta_j}) \left\langle y_j, u_0^{(s)} \right\rangle y_j(\boldsymbol{x}),$$

where $\langle \cdot, \cdot \rangle$ denotes the $L^2(\Omega)$ inner product. The definition of the Fourier transform gives

$$\widehat{\mathfrak{f}}(\sqrt{\theta_j})\cos(t\sqrt{\theta_j}) = \int_{-\infty}^{\infty} dt' \, \mathfrak{f}(t') \cos(t'\sqrt{\theta_j}) \cos(t\sqrt{\theta_j}) \\
= \frac{1}{2} \int_{-\infty}^{\infty} dt' \, \mathfrak{f}(t') \left\{ \cos\left[(t-t')\sqrt{\theta_j}\right] + \cos\left[(t+t')\sqrt{\theta_j}\right] \right\} \\
= \int_{-\infty}^{\infty} dt' \, \mathfrak{f}(t') \cos\left[(t-t')\sqrt{\theta_j}\right] = \mathfrak{f}(t) \star_t \cos(t\sqrt{\theta_j}),$$
(C.2)

where we used that f(t) is even. Equation (3.1) follows once we substitute this result in (C.1) and use the dominated convergence theorem, as in Appendix A, to take the time convolution out of the series. We also need the observation that

(C.3)
$$u^{(s)}(t, \boldsymbol{x}) = \cos\left[t\sqrt{A(c)}\right]u_0^{(s)}(\boldsymbol{x}) = \sum_{j=1}^{\infty}\cos\left(t\sqrt{\theta_j}\right)\left\langle y_j, u_0^{(s)}\right\rangle y_j(\boldsymbol{x}).$$

Appendix D. Proof of Proposition 4.1. We get from (2.25) and (3.1) that

$$D^{(r,s)}(t) - D^{(r,s)}(t; c_{\text{ref}}) = \int_{\Omega_{\text{in}}} d\boldsymbol{x} \, \rho(\boldsymbol{x}) \int_{-\infty}^{\infty} dt_1 \, u^{(s)}(t_1, \boldsymbol{x}) \int_0^t dt' \, \mathfrak{f}'(t' - t_1) \times G(t - t', \boldsymbol{x}, \boldsymbol{x}_r; c_{\text{ref}}),$$

where we used that $\operatorname{supp}(\rho) \subset \Omega_{\text{in}}$. Changing the variable of integration $t' = t_2 + t_1$ and using the notation

(D.1)
$$\psi(t, t_1, \boldsymbol{x}, \boldsymbol{x}_r) = \int_{-t_1}^{t-t_1} dt_2 f'(t_2) G(t - t_1 - t_2, \boldsymbol{x}, \boldsymbol{x}_r; c_{\text{ref}}),$$

we get

(D.2)
$$D^{(r,s)}(t) - D^{(r,s)}(t; c_{\text{ref}}) = \int_{\Omega_{\text{in}}} d\boldsymbol{x} \, \rho(\boldsymbol{x}) \int_{-\infty}^{\infty} dt_1 \, u^{(s)}(t_1, \boldsymbol{x}) \psi(t, t_1, \boldsymbol{x}, \boldsymbol{x}_r),$$

so let us study (D.1).

First, we note that since f'(t) is supported in $(-t_F, t_F)$, the right hand side in (D.1) vanishes when

$$(-t_1, t - t_1) \cap (-t_F, t_F) = \emptyset.$$

Thus, $\psi(t, t_1, \boldsymbol{x}, \boldsymbol{x}_r)$ is supported at $t_1 \in (-t_F, t + t_F)$, and (D.2) becomes, for t > 0,

(D.3)
$$D^{(r,s)}(t) - D^{(r,s)}(t; c_{\text{ref}}) = \int_{\Omega_{\text{in}}} d\boldsymbol{x} \, \rho(\boldsymbol{x}) \int_{-t_F}^{t+t_F} dt_1 \, u^{(s)}(t_1, \boldsymbol{x}) \psi(t, t_1, \boldsymbol{x}, \boldsymbol{x}_r).$$

Second, since the Green's function is supported at positive time arguments, we can rewrite the definition (D.1) as

$$\psi(t, t_1, \boldsymbol{x}, \boldsymbol{x}_r) = \int_{-\infty}^{\infty} dt_2 H(t_1 + t_2) f'(t_2) G(t - t_1 - t_2, \boldsymbol{x}, \boldsymbol{x}_r; c_{\text{ref}})$$

$$= \int_{-\infty}^{\infty} dt_3 H(t_3) f'(t_3 - t_1) G(t - t_3, \boldsymbol{x}, \boldsymbol{x}_r; c_{\text{ref}}),$$
(D.4)

where we recall that H(t) is the Heaviside step function. This solves the equation (recall Appendix A)

(D.5)
$$\left[\partial_t^2 + A(c_{\text{ref}})\right] \psi(t, t_1, \boldsymbol{x}, \boldsymbol{x}_r) = \partial_t \left[H(t) f'(t - t_1)\right] \delta_{\boldsymbol{x}_r}(\boldsymbol{x})$$

for $t \in \mathbb{R}$ and $x \in \Omega$, with homogeneous initial condition and with boundary condition

$$[1_{\partial\Omega_{D}}(\boldsymbol{x}) + 1_{\partial\Omega_{N}}(\boldsymbol{x})\partial_{n}]\psi(t,t_{1},\boldsymbol{x},\boldsymbol{x}_{r}) = 0, \quad t \in \mathbb{R}, \ \boldsymbol{x} \in \partial\Omega.$$

Since supp $f'(\cdot - t_1) \subset (t_1 - t_F, t_1 + t_F)$, the Heaviside function plays no role in the right hand side of (D.5) if $t_1 > t_F$ and we then get that $(t, \mathbf{x}) \mapsto \psi(t, t_1, \mathbf{x}, \mathbf{x}_r)$ is the solution to

(D.6)
$$\left[\partial_t^2 + A(c_{\text{ref}})\right] \psi(t, t_1, \boldsymbol{x}, \boldsymbol{x}_r) = \mathfrak{f}''(t - t_1) \delta_{\boldsymbol{x}_r}(\boldsymbol{x})$$

with $\psi(t, t_1, \boldsymbol{x}, \boldsymbol{x}_r) = 0$ for all t < 0. We can write

(D.7)
$$\psi(t, t_1, \boldsymbol{x}, \boldsymbol{x}_r) = \zeta^{(r)}(t - t_1, \boldsymbol{x}; c_{\text{ref}}),$$

where $\zeta^{(r)}(t, \boldsymbol{x}; c_{\text{ref}})$ is the analogue of the wave (2.6), the solution of (2.7)–(2.9), with $c(\boldsymbol{x})$ replaced by $c_{\text{ref}}(\boldsymbol{x})$ and F(t) replaced by f'(t). The even extension in time of this wave is $u^{(r)}(t, \boldsymbol{x}; c_{\text{ref}})$ and, similar to (2.17), we have for $t_1 > t_F$ and $t_1 < t - t_F$,

(D.8)
$$\psi(t, t_1, \mathbf{x}, \mathbf{x}_r) = \zeta^{(r)}(t - t_1, \mathbf{x}; c_{\text{ref}}) = \partial_t u^{(r)}(t - t_1, \mathbf{x}; c_{\text{ref}}).$$

In summary, the equation for computing the scattered wave at the receivers becomes

$$\begin{split} D^{(r,s)}(t) - D^{(r,s)}(t; c_{\text{ref}}) &= \int_{\Omega_{\text{in}}} d\boldsymbol{x} \, \rho(\boldsymbol{x}) \int_{-t_F}^{t+t_F} dt_1 \, u^{(s)}(t_1, \boldsymbol{x}) \psi(t, t_1, \boldsymbol{x}, \boldsymbol{x}_r) \\ &= \int_{\Omega_{\text{in}}} d\boldsymbol{x} \, \rho(\boldsymbol{x}) \int_{-t_F}^{0} dt_1 \, u^{(s)}(t_1, \boldsymbol{x}) \psi(t, t_1, \boldsymbol{x}, \boldsymbol{x}_r) \\ &+ \int_{\Omega_{\text{in}}} d\boldsymbol{x} \, \rho(\boldsymbol{x}) \int_{0}^{(t-t_F) \vee 0} dt_1 \, u^{(s)}(t_1, \boldsymbol{x}) \partial_t u^{(r)}(t - t_1, \boldsymbol{x}; c_{\text{ref}}) \\ &+ \int_{\Omega_{\text{in}}} d\boldsymbol{x} \, \rho(\boldsymbol{x}) \int_{(t-t_F) \vee 0}^{t+t_F} dt_1 \, u^{(s)}(t_1, \boldsymbol{x}) \psi(t, t_1, \boldsymbol{x}, \boldsymbol{x}_r). \end{split}$$

The first term in the right hand side vanishes because on the one hand the subdomain Ω_{in} is further than the distance $O(\bar{c}t_F)$ from the array, and on the other hand the hyperbolicity of the wave equation and the finite wave speed give that the support of $u^{(s)}(t_1, \boldsymbol{x})$ is disjoint from Ω_{in} for $|t_1| < t_F$. Consequently, we have

$$\begin{split} D^{(r,s)}(t) - D^{(r,s)}(t;c_{\mathrm{ref}}) &= \int_{\Omega_{\mathrm{in}}} d\boldsymbol{x} \, \rho(\boldsymbol{x}) \int_{0}^{t} dt_{1} \, u^{(s)}(t_{1},\boldsymbol{x}) \partial_{t} u^{(r)}(t-t_{1},\boldsymbol{x};c_{\mathrm{ref}}) \\ &- \int_{\Omega_{\mathrm{in}}} d\boldsymbol{x} \, \rho(\boldsymbol{x}) \int_{(t-t_{F})\vee 0}^{t} dt_{1} \, u^{(s)}(t_{1},\boldsymbol{x}) \partial_{t} u^{(r)}(t-t_{1},\boldsymbol{x};c_{\mathrm{ref}}) \\ &+ \int_{\Omega_{\mathrm{in}}} d\boldsymbol{x} \, \rho(\boldsymbol{x}) \int_{(t-t_{F})\vee 0}^{t+t_{F}} dt_{1} \, u^{(s)}(t_{1},\boldsymbol{x}) \psi(t,t_{1},\boldsymbol{x},\boldsymbol{x}_{r}). \end{split}$$

The last two terms in the right hand side vanish because the support of $\partial_t u_{\text{ref}}^{(r)}(t-t_1, \boldsymbol{x})$ and $\psi(t, t_1, \boldsymbol{x}, \boldsymbol{x}_r)$ is disjoint from Ω_{in} for $|t-t_1| < t_F$. Therefore, we have

(D.9)
$$D^{(r,s)}(t) - D^{(r,s)}(t; c_{\text{ref}}) = \int_{\Omega_{\text{in}}} d\boldsymbol{x} \, \rho(\boldsymbol{x}) \int_0^t dt_1 \, u^{(s)}(t_1, \boldsymbol{x}) \partial_t u^{(r)}(t - t_1, \boldsymbol{x}; c_{\text{ref}}).$$

Appendix E. Details on our implementation of the inversion algorithm. The data matrices (2.18) are generated by solving the initial boundary value problem (2.1)–(2.3) with a time domain, second-order centered finite-difference scheme in space and time, on a square mesh with size

$$h = \frac{\pi \bar{c}}{4(\omega_c + B)}.$$

The time steps in this scheme are chosen to satisfy the Courant–Friedreichs–Lewy condition.

The data driven mass matrix M is computed as in (3.25) and its block Cholesky square root R is obtained with [16, Algorithm 5.2]. We solve the wave equation in the reference medium with wave speed $c_{\text{ref}}(x)$ to compute the vector field $U(x; c_{\text{ref}})$ of snapshots and the reference data matrices $D(t; c_{\text{ref}})$, which then give $M(c_{\text{ref}})$ via (3.25). The block Cholesky square root $R(c_{\text{ref}})$ of $M(c_{\text{ref}})$ is computed with [16, Algorithm 5.2]. We use it to get $V(x; c_{\text{ref}}) = U(x; c_{\text{ref}})R(c_{\text{ref}})^{-1}$ and the estimated internal wave snapshots defined by (3.31).

The parametrization of the unknown $\rho(\mathbf{x})$ is done as in (4.3). At the *k*th iteration we have the estimate $\boldsymbol{\eta}^{(k)}$ of the vector of coefficients in the parametrization (4.3). This defines the estimate of the wave speed, as explained in section 4. To emphasize the dependence of this estimate on $\boldsymbol{\eta}^{(k)}$, we change the notation in this appendix to $\tilde{c}(\mathbf{x}; \boldsymbol{\eta}^{(k)})$. Each iteration seeks to update the vector of coefficients as

$$\boldsymbol{\eta}^{(k+1)} = \boldsymbol{\eta}^{(k)} + \delta \boldsymbol{\eta}.$$

where $\delta \eta$ is the minimizer of

(E.1)
$$\|\mathbf{\Gamma}(\boldsymbol{\eta}^{(k)})\delta\boldsymbol{\eta} - \boldsymbol{b}(\boldsymbol{\eta}^{(k)})\|_{2}^{2} + \mathscr{O}_{\text{reg}}(\boldsymbol{\eta}^{(k)} + \delta\boldsymbol{\eta}; \alpha^{(k)}).$$

The first term in this expression comes from the data fit term in the objective function, where the time and spatial integrals are approximated with the midpoint rule on the time grid with step τ and the spatial grid with step h. We arrange in lexicographical order the entries inside the Frobenius norm, for snapshot indexes j = 0, ..., n-1 and for source receiver pairs s, r = 1, ..., m. Then, the $\delta \eta$ independent term gives the vector $\mathbf{b}(\eta^{(k)}) \in \mathbb{R}^{m^2 n}$ and the matrix that multiplies $\delta \eta$ is $\Gamma(\eta^{(k)}) \in \mathbb{R}^{m^2 n \times N_{\rho}}$.

If we choose Tikhonov regularization,

(E.2)
$$\mathscr{O}_{\text{reg}}(\boldsymbol{\eta}^{(k)} + \delta \boldsymbol{\eta}; \alpha^{(k)}) = \alpha^{(k)} \|\delta \boldsymbol{\eta}\|_{2}^{2}$$

If we choose TV regularization, then we approximate

(E.3)
$$\mathscr{O}_{\text{reg}}(\boldsymbol{\eta}^{(k)} + \delta \boldsymbol{\eta}; \alpha^{(k)}) = \alpha^{(k)} \|\nabla \widetilde{c}(\boldsymbol{x}; \boldsymbol{\eta}^{(k)} + \delta \boldsymbol{\eta})\|_{L^{1}(\Omega_{\text{in}})},$$

via linearization of the map $\eta \mapsto \widetilde{c}(x;\eta)$ at $\eta^{(k)}$. We have from definitions (4.3) and (4.6) or (4.7) and the chain rule

(E.4)
$$\widetilde{c}(\boldsymbol{x}; \boldsymbol{\eta}^{(k)} + \delta \boldsymbol{\eta}) \approx \widetilde{c}(\boldsymbol{x}; \boldsymbol{\eta}^{(k)}) \left\{ 1 + \frac{1}{2} \left[1 + \frac{\widetilde{\rho}(\boldsymbol{x}; \boldsymbol{\eta}^{(k)})}{\sqrt{4 + \widetilde{\rho}^2(\boldsymbol{x}; \boldsymbol{\eta}^{(k)})}} \right] \sum_{j=1}^{N_{\rho}} \delta \eta_j \beta_j(\boldsymbol{x}) \right\},$$

where $\delta \boldsymbol{\eta} = (\delta \eta_1, \dots, \delta \eta_{N_\rho})^T$. The TV norm of this function is approximated using a standard approach (see, for example, [18]), and we obtain the following form of the regularization term,

(E.5)
$$\alpha^{(k)} \left\| \boldsymbol{\Psi}(\boldsymbol{\eta}^{(k)}) \delta \boldsymbol{\eta} + \boldsymbol{\xi}(\boldsymbol{\eta}^{(k)}) \right\|_{2}^{2},$$

for a full rank matrix $\Psi(\eta^{(k)})$, vector $\xi(\eta^{(k)})$, and redefined $\alpha^{(k)}$.

For both choices of the regularization, the estimation of $\delta\eta$ can now be rewritten as a linear least squares problem. For the Tikhonov regularization, the coefficient is chosen as

(E.6)
$$\alpha^{(k)} = (\gamma \sigma)^2, \qquad \sigma = \|\mathbf{\Gamma}(\boldsymbol{\eta}^{(k)})\|_2,$$

where σ is obviously the largest singular value of $\Gamma(\eta^{(k)})$ and γ is a user defined parameter. For the TV regularization, the coefficient is chosen using the generalized SVD of the pencil $[\Gamma(\eta^{(k)}), \Psi(\eta^{(k)})]$,

$$\mathbf{\Gamma}(\boldsymbol{\eta}^{(k)}) = \mathbf{Q}_1 \mathbf{\Sigma}_1 \mathbf{W}, \qquad \mathbf{\Psi}(\boldsymbol{\eta}^{(k)}) = \mathbf{Q}_2 \mathbf{\Sigma}_2 \mathbf{W},$$

where $\mathbf{Q}_{1,2}$ are unitary matrices, $\mathbf{\Sigma}_{1,2}$ are rectangular, diagonal matrices, and \mathbf{W} is a square matrix that is nonsingular (because $\mathbf{\Psi}(\boldsymbol{\eta}^{(k)})$ is supposed to be full rank). The matrix $\mathbf{\Sigma}_1$ has diagonal coefficients $0 \le \sigma_{\Gamma,1} \le \cdots \le \sigma_{\Gamma,N_{\rho}} \le 1$ (we assume $N_{\rho} \le m^2 n$) and the matrix $\mathbf{\Sigma}_2$ has diagonal coefficients $1 \ge \sigma_{\Psi,1} \ge \cdots \ge \sigma_{\Psi,N_{\rho}} > 0$ (we assume that the full rank matrix $\mathbf{\Psi}(\boldsymbol{\eta}^{(k)})$ has more rows than columns). The diagonal coefficients satisfy

$$\sigma_{\Gamma,j}^2 + \sigma_{\Psi,j}^2 = 1$$

for all j and the generalized singular values are the ratios $\sigma_{\Gamma,j}/\sigma_{\Psi,j}$ for $j=1,\ldots,N_{\rho}$. Note that the generalized singular values form an increasing sequence. We then choose

$$\alpha^{(k)} = (\gamma \sigma)^2, \qquad \sigma = \max_{j=1,\dots,N_{\rho}} \frac{\sigma_{\Gamma,j}}{\sigma_{\Psi,j}},$$

with a user defined γ .

The numerical results shown in section 5.1 are obtained with $\gamma = 0.03$ for the Tikhonov regularization and $\gamma = 0.01$ for the TV regularization. The numerical results shown in section 5.2 are obtained with TV regularization for $\gamma = 0.02$.

Acknowledgement. This material is based upon work supported by the Air Force Office of Scientific Research under award number FA9550-22-1-0077 to Borcea and Garnier, the U.S. Office of Naval Research under award number N00014-21-1-2370 to Borcea and Mamonov and the National Science Foundation under Grant No. DMS-2110265 to Zimmerling.

REFERENCES

- [1] Full Width at Half Maximum, Wolfram Math World, https://mathworld.wolfram.com/FullWidthatHalf Maximum.html (28 July 2022).
- [2] P. Benner, S. Gugercin, and K. Willcox, A survey of projection-based model reduction methods for parametric dynamical systems, SIAM Rev., 57 (2015), pp. 483–531.
- [3] B. BIONDI, 3D Seismic Imaging, Society of Exploration Geophysicists, Houston, TX, 2006.
- [4] L. BORCEA, V. DRUSKIN, A. MAMONOV, S. MOSKOW, AND M. ZASLAVSKY, Reduced order models for spectral domain inversion: Embedding into the continuous problem and generation of internal data, Inverse Problems, 36 (2020), 055010.
- [5] L. BORCEA, V. DRUSKIN, A. MAMONOV, AND M. ZASLAVSKY, Untangling the nonlinearity in inverse scattering with data-driven reduced order models, Inverse Problems, 34 (2018), 065008.
- [6] L. BORCEA, V. DRUSKIN, A. MAMONOV, AND M. ZASLAVSKY, Robust nonlinear processing of active array data in inverse scattering via truncated reduced order models, J. Comput. Phys., 381 (2019), pp. 1–26.
- [7] L. BORCEA, V. DRUSKIN, A. V. MAMONOV, M. ZASLAVSKY, AND J. ZIMMERLING, Reduced order model approach to inverse scattering, SIAM J. Imaging Sci., 13 (2020), pp. 685–723.
- [8] L. BORCEA, J. GARNIER, A. V. MAMONOV, AND J. ZIMMERLING, Reduced order model approach for imaging with waves, Inverse Problems, 38 (2021), 025004.
- [9] L. BORCEA, J. GARNIER, A. V. MAMONOV, AND J. ZIMMERLING, Waveform Inversion via Reduced Order Modeling, preprint, arXiv: 2202.01824, 2022, https://doi.org/10.1190/geo2022-0070.1.
- [10] R. BROSSIER, S. OPERTO, AND J. VIRIEUX, Velocity model building from seismic reflection data by full-waveform inversion, Geophys. Prospect., 63 (2015), pp. 354–367.
- [11] S. Brunton and J. Kutz, Data-Driven Science and Engineering: Machine Learning, Dynamical Systems, and Control, Cambridge University Press, Cambridge, 2019.
- [12] F. CAKONI, D. COLTON, AND P. MONK, The Linear Sampling Method in Inverse Electromagnetic Scattering, SIAM, Philadelphia, 2011.
- [13] M. CHENEY AND B. BORDEN, Fundamentals of Radar Imaging, SIAM, Philadelphia, 2009.
- [14] J. Curlander and R. McDonough, Synthetic Aperture Radar: Systems and Signal Processes, Wiley Ser. Remote Sensing 11, Wiley, New York, 1991.
- [15] V. DRUSKIN, A. V. MAMONOV, A. E. THALER, AND M. ZASLAVSKY, Direct, nonlinear inversion algorithm for hyperbolic problems via projection-based model reduction, SIAM J. Imaging Sci., 9 (2016), pp. 684–747.
- [16] V. DRUSKIN, A. V. MAMONOV, AND M. ZASLAVSKY, A nonlinear method for imaging with acoustic waves via reduced order model backprojection, SIAM J. Imaging Sci., 11 (2018), pp. 164–196.
- [17] V. DRUSKIN, S. MOSKOW, AND M. ZASLAVSKY, Lippmann-Schwinger-Lanczos algorithm for inverse scattering problems, Inverse Problems, 37 (2021), 075003.

- [18] S. GAZZOLA AND M. SABATÉ LANDMAN, Flexible GMRES for total variation regularization, BIT, 59 (2019), pp. 721–746.
- [19] S. HERKT, M. HINZE, AND R. PINNAU, Convergence analysis of Galerkin pod for linear second order evolution equations, Electron. Trans. Numer. Anal., 40 (2013), pp. 321–337.
- [20] J. Hesthaven, G. Rozza, and B. Stamm, Certified Reduced Basis Methods for Parametrized Partial Differential Equations, Springer, New York, 2016.
- [21] G. Huang, R. Nammour, and W. Symes, Source-independent extended waveform inversion based on space-time source extension: Frequency-domain implementation, Geophysics, 83 (2018), pp. R449– R461
- [22] F. JOHN, Partial Differential Equations, 4th ed., Springer, New York, 1982.
- [23] A. KIRSCH AND N. GRINBERG, The Factorization Method for Inverse Problems, Oxford Lecture Ser. Math. Appl. 36, Oxford University Press, Oxford, 2007.
- [24] K. Kunisch and S. Volkwein, Optimal snapshot location for computing POD basis functions, ESAIM Math. Model. Numer. Anal., 44 (2010), pp. 509–529.
- [25] Y. MA AND D. HALE, Wave-equation reflection traveltime inversion with dynamic warping and full-waveform inversion, Geophysics, 78 (2013), pp. R223–R233.
- [26] I. MASONI, J. BOELLE, R. BROSSIER, AND J. VIRIEUX, Layer stripping FWI for surface waves, in SEG Technical Program Expanded Abstracts 2016, Society of Exploration Geophysicists, Houston, TX, 2016, pp. 1369–1373.
- [27] R.-E. Plessix, A review of the adjoint-state method for computing the gradient of a functional with geophysical applications, Geophys. J. Int., 167 (2006), pp. 495–503.
- [28] W. SYMES, Migration velocity analysis and waveform inversion, Geophys. Prospect., 56 (2008), pp. 765–790.
- [29] W. Symes and J. Carazzone, Velocity inversion by differential semblance optimization, Geophysics, 56 (1991), pp. 654–663.
- [30] D. Verschuur, Seismic Multiple Removal Techniques: Past, Present and Future, EAGE Publications, Houten, The Netherlands, 2013.
- [31] J. VIRIEUX AND S. OPERTO, An overview of full-waveform inversion in exploration geophysics, Geophysics, 74 (2009), pp. WCC1–WCC26.
- [32] A. Weglein, F. Gasparotto, P. Carvalho, and R. Stolt, An inverse-scattering series method for attenuating multiples in seismic reflection data, Geophysics, 62 (1997), pp. 1975–1989.
- [33] Y. Yang, B. Engquist, J. Sun, and B. Hamfeldt, Application of optimal transport and the quadratic Wasserstein metric to full-waveform inversion, Geophysics, 83 (2018), pp. R43–R62.